Analytical model of the network topology and rigidity of calcium aluminosilicate glasses

Yang, Kai; Hu, Yushu; Li, Zhou; Krishnan, N. M. Anoop; Smedskjær, Morten Mattrup; Hoover, Christian G.; Mauro, John C.; Sant, Gaurav; Bauchy, Mathieu

Published in:
Journal of the American Ceramic Society

DOI (link to publication from Publisher):
10.1111/jace.17781

Publication date:
2021

Document Version
Accepted author manuscript, peer reviewed version

PROFESSOR N. M. ANOOP KRISHNAN (Orcid ID : 0000-0003-1500-4947)

DR MORTEN SMEDSKJAER (Orcid ID : 0000-0003-0476-2021)

DR JOHN C. MAURO (Orcid ID : 0000-0002-4319-3530)

DR MATHIEU BAUCHY (Orcid ID : 0000-0003-4600-0631)

Article type : Article

Analytical Model of the Network Topology and Rigidity of Calcium Aluminosilicate Glasses

Kai Yang[1], Yushu Hu[1], Zhou Li[1], N M Anoop Krishnan[2, 3], Morten M. Smedskjaer[4], Christian G. Hoover[5], John C. Mauro[6], Gaurav Sant[7, 8, 9], Mathieu Bauchy[1,9] *

[1]Physics of AmoRphous and Inorganic Solids Laboratory (PARISlab), University of California, Los Angeles, California 90095, USA

[2]Department of Civil Engineering, Indian Institute of Technology Delhi, Hauz Khas, New Delhi 110016, India

[3]Department of Material Science and Engineering, Indian Institute of Technology Delhi, Hauz Khas, New Delhi 110016, India

[4]Department of Chemistry and Bioscience, Aalborg University, 9220 Aalborg, Denmark

[5]School of Sustainable Engineering and the Built Environment, Arizona State University, Tempe, Arizona 85287, USA

[6]Department of Materials Science and Engineering, Pennsylvania State University, University Park, Pennsylvania 16802, USA

[7]Laboratory for the Chemistry of Construction Materials (LC[2]), Department of Civil and Environmental Engineering, University of California, Los Angeles, California 90095, USA

[8]Department of Materials Science and Engineering, University of California, Los Angeles, California 90095, USA

[9]Institute for Carbon Management, University of California, Los Angeles, California 90095, USA

*Corresponding author: Prof. Mathieu Bauchy, bauchy@ucla.edu

Abstract

Topological constraint theory (TCT) has enabled the prediction of various properties of oxide glasses as a function of their composition and structure. However, the robust application of TCT relies on accurate knowledge of the network structure and topology. Here, based on classical molecular dynamics simulations, we derive a fully analytical model describing the topology of the calcium aluminosilicate [$(CaO)_x(Al_2O_3)_y(SiO_2)_{1-x-y}$, CAS] ternary system. This model yields the state of rigidity (flexible, isostatic, or stressed-rigid) of CAS systems as a function of composition and temperature. These results reveal the existence of correlations between network topology and glass-forming ability. This study suggests that glass-forming ability is encoded in the network topology of the liquid state rather than that of the glassy state.

Keywords

Topological constraint theory, Molecular dynamics, Calcium aluminosilicate

1. Introduction

The **calcium aluminosilicate (CAS)** system is an archetypical model for alkali-free glasses used in display applications[1] and cementitious materials (e.g., cement, fly ash, or slag).[2] The structure and properties of the CAS ternary system have been extensively studied from experiments,[3–6] atomistic simulations,[7–10] and machine learning.[11–13] Indeed, this ternary system offers an ideal model to investigate the effects of polymerization (i.e., by varying the Ca/Al ratio) and of the network-forming skeleton (i.e., by varying the Al/Si ratio at fixed Ca/Al).

Since the stoichiometry of CAS and other oxide glasses can be continuously adjusted, there exists a largely untapped opportunity to discover new glass compositions featuring desirable properties and functionalities.[14, 15] However, the vastness of the accessible compositional space renders traditional material discovery approaches (e.g., Edisonian "trial-and-error") inefficient.[16] In that regard, composition-property predictive models can facilitate and rationalize the search for new glasses by targeting searches toward promising compositional domain.[17, 18]

To this end, **topological constraint theory (TCT)** has been a key enabler to develop predictive models that relate the composition and structure of glasses to their properties.[19, 20] Various TCT-based models have been proposed over the past decades to predict glass-forming ability, glass transition temperature, liquid fragility, hardness, stiffness, dissolution rate, etc.[19, 21–28] The success of TCT is based on the fact that many macroscopic properties of disordered materials primarily depend on the topology of the atomic structure, while other structural details only have a second-order effect.[29] As such, TCT reduces complex disordered atomic networks into simpler structural trusses,[22] wherein some nodes (the atoms) are connected to each other by some topological constraints (the chemical bonds). In structural glasses, topological constraints comprise of the radial two-body **bond-stretching (BS)** and angular three-body **bond-bending (BB)** constraints. The **number of constraints per atom (n_c)** then offers a simple, reduced-dimensionality metric that is often correlated with macroscopic properties.[22]

Importantly, predictions from TCT critically rely on an accurate knowledge of the glass structure and connectivity, which is the key to enumerate the number of BS and BB constraints created by each type of atoms in the glass network.[30] This is a challenge as the local structure of glasses (and hence, the number of constraints) changes as a function of composition. For instance, CAS glasses exhibit several structural complexities, e.g., overcoordinated Al atoms,[5, 31–33] tricluster oxygen units,[34] free oxygen species,[35, 36] varying Ca environments,[37] etc. All of these features impact the constraints enumeration and, hence, should be accounted for in robust topological models. Although such information can be accessed by **molecular dynamics (MD)** simulations of one composition at a time,[30] it is not practical to systematically conduct MD simulations over large compositional domains considering their high computational cost. In addition, discrete models (e.g., relying on a finite, discrete number of MD simulations) are not differentiable, that is, they do not allow for the computation of the derivative of the number of constraints per atom with respects to composition.[38] This prevents the use of gradient-based "inverse design" optimization methods (e.g., to pinpoint glasses with minimum, maximum, or tailored rigidity).

Here, to address these challenges, we present a fully analytical model describing the network topology of $(CaO)_x(Al_2O_3)_y(SiO_2)_{1-x-y}$ (CAS) glasses over the entire ternary domain. This

model is informed and validated by a series of classical MD simulations, but, importantly, offers a pathway to continuously predict the properties of CAS glasses as a function of their compositions without the need for any systematic MD simulation.

This paper is organized as follows. Section 2 describes the MD simulations used in this study. We then introduce our analytical topological model for CAS glasses in Sec. 3. In Sec. 4, we discuss the obtained rigidity diagrams of the CAS ternary system. Finally, we establish some conclusions in Sec. 5.

2. Methods

To establish our analytical model, we first conduct MD simulations of 231 CAS glasses using the Large-scale Atomic/Molecular Massively Parallel Simulator (LAMMPS) package.[39] The chosen compositions homogeneously cover the entire CAS domain, with 5% increments in the mol% concentration of the CaO, Al_2O_3 and SiO_2 oxide constituents. Note that some of these CAS glasses do not exhibit satisfactory glass-forming ability in practice, but they all can be generated by MD due to the use of a high cooling rate. Each glass sample comprises around 3000 atoms. This system size is found to be large enough to ensure that the computed structural features presented in the following are not affected by any finite size effect (see Supplemental Material).

Here, we adopt the interatomic potential parametrized by Jakse,[8] which has been reported to offer good results in agreement with experiment data[34, 40, 41] and applied in several previous studies.[11, 42] The Jakse potential relies on partial charges and a 2-body Born-Mayer-Huggins formulation:

$$U_{ij}(r_{ij}) = \frac{q_i q_j}{4\pi\epsilon_0 r_{ij}} + A_{ij}\exp\left(\frac{\sigma_{ij} - r_{ij}}{\rho_{ij}}\right) - \frac{C_{ij}}{r_{ij}^6} \qquad \text{(Eq. 1)}$$

where i and j refers to pairs of elements (Si, O, Al, and Ca), r_{ij} is the distance between atom i and j, q_i and q_j are the partial charges of elements i and j, ϵ_0 is the vacuum dielectric permittivity, and A_{ij}, σ_{ij}, ρ_{ij}, and C_{ij} are some fitting parameters [Tab. 1]. A cutoff of 8.0 Å is used for the short-range interactions. The Coulombic interactions are calculated by adopting the Fennell damped shifted force field model with a damping parameter of 0.25 $Å^{-1}$ and a global cutoff of 8.0 Å.[43] We keep the integration timestep as fixed as 1.0 fs.

We generate the CAS glass samples using the conventional melt-quench method, as described in the following.[44] First, atoms are randomly placed in a cubic box using PACKMOL with a distance cutoff of 2.0 Å between each pair of atoms to avoid any unrealistic overlap.[45] It is worth noting that the choice of the initial density of the system is irrelevant since, after being homogenized at elevated temperature, the melt fully loses the memory of its initial configuration (and of its initial density). These initial configurations are then subjected to an energy minimization process, followed by 100 ps relaxations in the canonical (*NVT*) and isothermal-isobaric (*NPT*) ensembles at 300 K, sequentially. These samples are then fully melted at 3000 K for 100 ps in the *NVT* and, subsequently, *NPT* ensemble (at zero pressure) to ensure the loss of the memory of the initial configurations and to equilibrate the systems. Next, these liquids are cooled from 3000 K to 300 K in the *NPT* ensemble at zero pressure with a cooling rate of 1 K/ps. The obtained glass samples are further relaxed at 300 K for 100 ps in the *NPT* ensemble—so that the simulated glasses are eventually representative of experimental glasses at room temperature. This relaxation is long enough to ensure a plateau in the energy and volume of the simulated glasses (see Supplemental Material). Note that this quenching procedure is slightly adjusted for the following select compositions: (1) a higher initial melting temperature of 5000 K is used for the samples wherein the SiO_2 concentration is larger or equal to 95 mol%—since these glasses exhibit high glass transition temperatures, and (2) a faster cooling rate of 100 K/ps is used for the samples wherein the CaO concentration is larger or equal to 90 mol%. Indeed, although the cooling rate can affect the glass structure, the use of a higher cooling rate here is necessary as these systems would otherwise tend to crystallize with a cooling rate of 1 K/ps.

Once relaxed, the glasses are subjected to a structural analysis. We compute the coordination number of each atom by enumerating the number of neighbors that are present in their first coordination shell. The extent of the first coordination shell of each element is taken as the distance associated with the first minimum after the first peak in the partial pair distribution functions. This yields a cutoff of 2.000, 2.345, and 3.045 Å for Si–O, Al–O, and Ca–O bonds, respectively. We then label Al atoms as being 4- or 5-fold coordinated if they have 4 or 5 O neighbors in their first coordination shell, respectively. Similarly, we enumerate for each O atom the number of network-forming species (Si or Al) that are present in their first coordination

shell (based on the previous cutoff values). Oxygen atoms are then labeled as **free oxygen (FO)**, **non-bridging oxygen (NBO)**, **bridging oxygen (BO)** or **tri-cluster oxygen (TO)** if they present 0, 1, 2, or 3 network-forming neighbors in their first coordination shell, respectively.

For statistical purposes, six independent quenching simulations are performed for each glass. All the data presented in the following are averaged over these repetitions. The average standard deviation associated with each computed property is presented in Supplemental Material.

3. Topological model of calcium aluminosilicate glasses

1. Polymerization and depolymerization of the aluminosilicate network

a. Effect of Ca and Al atoms on topology

To establish our topological model of CAS glasses, we take as a reference the structure of glassy silica (SiO_2), wherein all the Si and O atoms are 4- and 2-fold coordinated, respectively—that is, all the O act as bridging oxygen atoms bonded to two network formers.[14] Starting from this reference structure, we then describe the competitive effects of Ca and Al atoms: (i) each Ca atom consumes 2 BOs and, in turn, creates 2 non-bridging oxygen atoms,[46] whereas, in contrast, (ii) each Al atom consumes 1 NBO and creates 1 BO.[14] These well-known effects arise from the following mechanisms. On one hand, when added to pure SiO_2, Ca^{2+} cations act as network modifiers as they tend to depolymerize the atomic network by breaking some Si–O–Si inter-tetrahedral joints and, in turn, charge-compensating pairs of negatively-charged NBOs.[46] On the other hand, starting from a calcium silicate glass, newly-added Al atoms act as network formers and tend to repolymerize the network by using available Ca^{2+} cations to charge-compensate negatively-charged 4-fold coordinated AlO_4 units.[47–50] This effectively increases the network connectivity since the Ca cations that are used as charge compensators do not create any NBO any longer. Based on this model, the number of BO (N_{BO}) and NBO (N_{NBO}) are expressed as:

$$N_{\mathrm{BO}} = N_{\mathrm{O}} - 2 \times N_{\mathrm{Ca}} + N_{\mathrm{Al}} \quad \text{(Eq. 2)}$$

$$N_{\mathrm{NBO}} = 2 \times N_{\mathrm{Ca}} - N_{\mathrm{Al}} \quad \text{(Eq. 3)}$$

where N_{BO}, N_{NBO}, N_{O}, N_{Ca}, and N_{Al} are the number of BO, NBO, total oxygen, calcium, and aluminum atoms, respectively. Note that these equations are not valid for all CAS compositions. In detail, mechanism (i) can hold until the added Ca atoms exhaust all the BOs present in the network, that is, for $N_{\mathrm{BO}} \geq 0$, while mechanism (ii) remains possible until the added Al atoms consume all the NBOs present in the network, that is, for $N_{\mathrm{NBO}} \geq 0$. In the following sections, we discuss the cases of the Ca-rich regime (i.e., when mechanism (i) is no longer possible) and Al-rich regime (i.e., when mechanism (ii) breaks down).

Figure 1 illustrates and summarizes the overall network connectivity in CAS glasses—and its dependance on glass composition. Starting from a reference $(CaO)_{25}(SiO_2)_{75}$ binary calcium silicate glass [Fig. 1(a)], the addition of CaO tends to decrease polymerization—since, as a network modifier, Ca atoms tend to break Si–O bonds and result in the formations of NBOs [Fig. 1(b)]. In contrast, the addition of Al_2O_3 tends to increase polymerization—since Al atoms tend to "consume" NBOs by using Ca atoms as charge-compensating species [Fig. 1(c)].

b. Ca-rich regime: formation of free oxygen atoms

We then focus on the Ca-rich regime (i.e., wherein N_{BO} would become negative assuming that Eq. 2 would continue to hold) and discuss the effect of Ca atoms on the network topology in this compositional domain. In this domain, the network becomes fully depolymerized, that is, there is no remaining BO and all Si and Al polytopes are isolated from each other. In this regime, our MD simulations suggest that the excess of Ca atoms results in the formation of free oxygen atoms [Fig. 3(a)], that is, O atoms that are not connected to any Si or Al network former.[42] This echoes previous experimental findings that also suggested the existence of FOs.[35, 36, 52]

Based on this observation, we describe the number of FO atoms according to the following model. First, we assume that, in this regime, all the Si and Al atoms remain 4-fold coordinated and, hence, they are each surrounded by 4 NBOs. The number of NBOs is then given by:

$$N_{\mathrm{NBO}} = 4 \times (N_{\mathrm{Si}} + N_{\mathrm{Al}}) \qquad \text{(Eq. 4)}$$

We then assume that all the remaining O atoms act as FOs, whose number is given by:

$$N_{\mathrm{FO}} = N_{\mathrm{O}} - N_{\mathrm{NBO}} \quad \text{(Eq. 5)}$$

c. Al-rich regime: formation of 5-fold aluminum and tricluster oxygen atoms

Next, we focus on the Al-rich regime (i.e., $2N_{\mathrm{Ca}} < N_{\mathrm{Al}}$, wherein N_{NBO} would become negative assuming that Eq. 3 would continue to hold) and discuss how additional Al^{3+} cations impact the atomic structure of CAS glasses. In this domain, the glass compositions are peraluminous, that is, they exhibit an excess number of Al atoms as compared to the ones that are needed to charge-compensate all the calcium atoms in the glass (i.e., $N_{\mathrm{Al}} = 2N_{\mathrm{Ca}}$).[46] In this regime, all the AlO_4 tetrahedral units cannot be charge-compensated any longer due to the deficit of Ca cations. From this point, two possible mechanisms have been suggested to occur: (i) some Al atoms become overcoordinated (i.e., with a coordination number larger than 4) and (ii) some 3-fold coordinated triclusters oxygen atoms (i.e., O atoms that are connected to 3 Si or Al network formers) tend to form.[34, 53, 54] We now discuss these two behaviors.

First, previous experiments[5, 31–33] and simulations[11, 42] have suggested that some excess Al atoms become overcoordinated, that is, they become 5- or 6-fold coordinated. Neuville *et al.* reported the existence of a small fraction (< 3%) of 6-fold coordinated aluminum (Al^{VI}) at very high Al/Ca ratios, in agreement with our MD simulations.[11] However, here, considering that independently predicting the fractions of both 5- and 6-fold coordinated Al atoms would be ill-defined based on the present assumptions, we assume that the fraction of 6-fold coordinated Al is small enough to be neglected—that is, we assume that, in this regime, all the overcoordinated Al atoms are 5-fold coordinated.

Figure 2 shows the composition dependence of the number of predicted and computed 5-fold Al atoms per formula unit of glass for $(CaO)_x(Al_2O_3)_y(SiO_2)_{1-x-y}$, as a function of $[Al_2O_3]$ – [CaO] (since this metric is found to be the most influential overall). As expected, we find that the number of overcoordinated Al remains nearly zero as long as there is no deficit of Ca cations (i.e., $2N_{\mathrm{Ca}} > N_{\mathrm{Al}}$). Although our analytical model predicts the number of 5-fold Al atoms to be strictly zero in fully-compensated glasses (i.e., wherein $[Al_2O_3]$ = [CaO]), MD simulations do predict the

existence of a small fraction of such overcoordinated atoms even when [Al_2O_3] < [CaO]. This echoes previous experiments.[5, 55] This is a consequence of the fact that our model relies on an ideal representation of the glass structure, wherein all Al atom remain 4-fold coordinated if they can be charge-compensated by a Ca cation. However, simulated glasses tend to slightly deviate from this ideal representation, since they present a small fraction of 5-fold Al atoms even when Al atoms could theoretically remain 4-fold coordinated. This increased disorder observed in simulated glasses is a consequence of entropic effects associated with the high cooling rate used during their quenching. Although our analytical model presently does not account for such entropic effects, this limitation does not notably impact its ability to reliably predict the topology of CAS glasses (see below) since the fraction of excess 5-fold coordinated Al atoms remains low (less than 8%). Hence, this small fraction of excess 5-fold coordinated Al atoms is neglected from our model thereafter.

We then find that the computed number of 5-fold coordinated Al atoms scales fairly linearly with the number of excess Al atoms (i.e., $N_{\mathrm{Al}} - 2N_{\mathrm{Ca}}$), which suggests that the number of overcoordinated Al is proportional to the number of excess Al atoms. Based on this observation, we model the number of 5-fold coordinated Al atoms ($N_{\mathrm{Al^V}}$) as:

$$N_{\mathrm{Al^V}} = \alpha(N_{\mathrm{Al}} - 2 \times N_{\mathrm{Ca}}) \qquad \text{(Eq. 6)}$$

where α is an empirical factor that captures the fraction of excess Al that eventually becomes overcoordinated. Here, based on our MD results, we assume that a quarter of the excess Al atoms become overcoordinated (i.e., $\alpha = 1/4$), which yields a good match between MD simulations and the present analytical model [Fig. 2]. This specific value of α here is chosen based on the fact that, even though it slightly overestimates the number of 5-fold coordinated Al atoms, it partially compensates for the fact that our model is neglecting 6-fold coordinated Al atoms (see below).

The fact that the number of 5-fold coordinated Al atoms is lower than the number of excess Al atoms (i.e., that are not charge-compensated by Ca atoms) suggests that there is another charge compensation mechanism at play in the Al-rich regime, namely, through the

formation of TO atoms. Indeed, our MD simulations show the existence of such TO species, which echoes previous experiments and simulations.[34, 53, 54] We model the number of TO atoms as follows.

To determine the fraction of TO atoms in the glass, we first calculate the total excess negative charge of all 4- and 5-fold coordinated Al atoms that are not charge-compensated by Ca atoms and subsequently determine the number of TO atoms that is needed to counterbalance the excess negative charge. We first calculate the excess negative charge of AlO_4 and AlO_5 units by assuming that all the O atoms take the form of BOs in these polytopes (i.e., each O contributes a charge of –1 to the central Al). This analysis yields an overall local charge of –1 and –2 for AlO_4 and AlO_5 units, respectively, so that the total excess negative charge is $(N_{\mathrm{Al^{IV}}} - 2 \times N_{\mathrm{Ca}}) + 2 \times N_{\mathrm{Al^{V}}}$, where $N_{\mathrm{Al^{IV}}}$ is the number of 4-fold coordinated Al atoms. In turn, replacing a BO by a TO in the Al polytopes increases the local charge by +1/3 since a BO contributes a charge of –1 to the central Al (i.e., –2/2), whereas a TO only contributes a charge of –2/3 since it is shared by three Si or Al polytopes.[56] Altogether, since a TO is connected to 3 distinct polytopes, the overall increase in charge resulting from the transformation of a BO into a TO is equal to +1 (i.e., $3 \times 1/3$). Based on this, the number of TO atoms that is needed to counterbalance the excess negative charge of the Al atoms is then given by:

$$N_{\mathrm{TO}} = N_{\mathrm{Al^{IV}}} + 2 \times N_{\mathrm{Al^{V}}} - 2 \times N_{\mathrm{Ca}} \qquad \text{(Eq. 7)}$$

where N_{TO} is the number of TO atoms. Since our model assumes the existence of only 4- and 5-fold coordinated Al atoms in the Al-rich regime, Eq. 7 can be converted into:

$$N_{\mathrm{TO}} = N_{\mathrm{Al}} - 2 \times N_{\mathrm{Ca}} + N_{\mathrm{Al^{V}}} \qquad \text{(Eq. 8)}$$

We then assume that all the remaining O atoms act as BOs in Al-rich regime, whose number is given by:

$$N_{\mathrm{BO}} = N_{\mathrm{O}} - N_{\mathrm{TO}} \qquad \text{(Eq. 9)}$$

d. Comparison between analytical model and MD simulations

To validate the ability of our analytical model to offer accurate predictions of the degree of connectivity in the CAS glasses, we now compare the oxygen species fractions (i.e., in order of increasing connectivity: FO, NBO, BO, and TO) predicted by our model with those computed by MD simulations. Table 2 summarizes the predicted fractions for each oxygen species as a function of the molar fractions of CaO and Al_2O_3 (*x* and *y* respectively) following the unit formula $(CaO)_x(Al_2O_3)_y(SiO_2)_{1-x-y}$. Equations are provided for: (1) "*fully-depolymerized regime*," i.e., wherein all BOs are consumed by Ca atoms, so that the glass network only comprises of FO and NBO atoms (i.e., $(y - x) \leq -2/3$), (2) "*partially-depolymerized regime*," wherein the network only contains NBO and BO atoms (i.e., $-2/3 \leq (y - x) \leq 0$), and (3) "*fully-polymerized regime*," wherein the network only contains BO and TO atoms (i.e., $0 \leq (y - x)$).

Figure 3 shows the comparison between predicted (by our analytical model) and computed (by MD simulations) fractions for the oxygen species (a) FO, (b) NBO, (c) BO, and (d) TO as a function of $[Al_2O_3]$ – [CaO]. We first note that our analytical model offers good predictions of FO, NBO, BO, and TO over the entire CAS domain, both in terms of trend and magnitude. Then, we also note that our analytical model solely depends on the competition between $[Al_2O_3]$ and [CaO] atoms (i.e., "*y – x*", see Tab. 3) and, hence, does not fully capture the variations in the fractions of oxygen species at a fixed value of "*y – x.*" The deviations between model and MD simulations are mostly observed at the vicinity of the transitions between compositional regimes, namely, near the fully-compensated (i.e., $y - x = 0$) and fully-depolymerized domains (i.e., $y - x = -2/3$). Specifically, we find that the MD simulations predict a non-zero fraction of FO, NBO, BO, and TO even when the fractions of such species are predicted to be strictly zero. Such discrepancies can be attributed to the fact that, for the sake of simplification, our model assumes that only two types of oxygen species can coexist at the same time, while experiments[35, 52, 54] and MD simulations[34, 42] suggest that more than two species can simultaneously coexist in the network. As mentioned above, this slight discrepancy is a consequence of the fact that our model relies on ideal assumptions in order to remain simple and analytical (e.g., TO atoms are not

formed as long as all the 4-fold coordinated Al atoms can be charge-compensated by Ca atoms). In contrast, simulated glasses tend to exhibit some enhanced degree of disorder, which arises from entropic effects that are not accounted for by our model. Nevertheless, the difference between the simulated and predicted fractions of O species remains small and, hence, does not notably impact the ability of our model to reliably predict the topology of CAS glasses (see below). Nevertheless, despite these simplifications, our model offers a realistic description of the overall degree of connectivity of the glass, which is key to analytically predict the number of constraints per atom in the network (see Sec. 4). We emphasize that this level of agreement is not the result of any fitting and, rather, is a direct consequence of the physical/chemical mechanisms described in Sec. 3.1. Clearly, an enhanced agreement could be obtained with simply fitting the MD data with a complex non-linear function, but this approach would lack any physical foundation.

2. Connectivity of the network modifiers

We now discuss how the local connectivity of the network-modifying atoms (i.e., Ca atoms) is varying as a function of the glass composition. The analytical model described in the following aims to predict the partial coordination numbers of Ca atoms, that is, the average number of FO, NBO, BO, and TO around each Ca atom—which is critical to inform our topological model (see Sec. 4).

To establish our model of Ca connectivity, we take an alternative viewpoint and start by describing the average number of Ca around each type of O species. Indeed, based on the analysis of our MD simulations, we find that the average number of Ca atoms around FO, NBO, BO, and TO atoms remains fairly constant and barely depends on glass composition. The average FO–Ca, NBO–Ca, BO–Ca, and TO–Ca partial coordination numbers ($\bar{r}_{\mathrm{XO-Ca}}$, wherein XO refers to a given O species) are equal to 5.5, 3.0, 0.78, and 0.12, respectively. This trend (i.e., $\bar{r}_{\mathrm{FO-Ca}} > \bar{r}_{\mathrm{NBO-Ca}} > \bar{r}_{\mathrm{BO-Ca}} > \bar{r}_{\mathrm{TO-Ca}}$) can be understood from the fact that, starting from an isolated FO, the addition of each O–Si or O–Al bond (i) reduces the need for the negative charge of O atoms to be compensated by the nearby presence of a Ca cation and (ii) occupies some space around the central O, which prevents the accumulation of Ca neighbors. These partial coordination numbers

can also be understood as a degree of "affinity" between Ca atoms and O species, wherein Ca cations are preferentially located in the vicinity of FO atoms and almost fully avoid TO atoms.

The knowledge of the XO–Ca partial coordination numbers then allows us to determine the Ca–XO coordination numbers ($r_{\mathrm{Ca-XO}}$) by expressing the total number of Ca–XO bonds ($N_{\mathrm{Ca-XO}}$) in two different ways as:

$$N_{\mathrm{Ca-XO}} = N_{\mathrm{Ca}} \times r_{\mathrm{Ca-XO}} = N_{\mathrm{XO}} \times r_{\mathrm{XO-Ca}} \quad \text{(Eq. 10)}$$

where N_{XO} is the number of XO atoms (where XO = FO, NBO, BO, and TO). As an additional refinement of the model, we add a scaling coefficient β to ensure that the total average coordination number of Ca cations (i.e., the sum of all the partial Ca–XO coordination numbers) remains equal to 6 throughout the entire CAS compositional domain:[57]

$$r_{\mathrm{Ca-XO}} = \beta \frac{N_{\mathrm{XO}} \times \bar{r}_{\mathrm{XO-Ca}}}{N_{\mathrm{Ca}}} \quad \text{(Eq. 11)}$$

where β can be expressed as:

$$\beta = \frac{6}{\sum_{\mathrm{XO}} (\bar{r}_{\mathrm{XO-Ca}} \times N_{\mathrm{XO}}) / N_{\mathrm{Ca}}} \quad \text{(Eq. 12)}$$

where the summation spans over all the O species (XO = FO, NBO, BO, and TO).

Figure 4 shows a comparison between the calculated (i.e., by our analytical model) and computed (i.e., by MD simulations) values of the (a) Ca–FO, (b) Ca–NBO, (c) Ca–BO, and (d) Ca–TO partial coordination numbers as a function of $[Al_2O_3]$ – [CaO]. Despite relying on simple assumptions, our model yields realistic predictions, both in terms of trend and magnitude. Similar to Fig. 3, we observe that most of the deviations between our model and MD simulations occur in the vicinity of the transitions between the fully-compensated and fully-depolymerized domains—again a consequence of the fact that our model only assumes that at most two types of oxygen species can coexist at the same time. Finally, we note that the computed Ca–XO partial

coordination numbers exhibit some slight variations at fixed value of $[Al_2O_3]$ – [CaO], which is not accounted for by our model. Nevertheless, it is notable that the present analytical model can capture fairly well the non-monotonic and non-linear evolution of the local connectivity around Ca atoms while only relying on simple assumptions regarding the relative affinity of FO, NBO, BO, and TO atoms for Ca cations.

Overall, based on Eqs. 4-to-12, our model can predict the average network topology of CAS glasses by using the glass composition as sole input—which is key to analytically predict the number of constraints per atom as a function of composition. Since it solely depends on composition, our analytical model is intrinsically unable to capture the potential existence of topological fluctuations at fixed composition. Nevertheless, we note that, based on the analysis of the structure of the glasses generated independent quenching, the variability in the glass connectivity at fixed composition never exceeds 1% (see Tab. S2 in the Supplemental Material). As such, our model can reliably predict the average (i.e., configurational average) topology of CAS glasses as a function of their composition.

4. Rigidity diagram of the calcium aluminosilicate ternary system

1. Glassy state

We use the topological inputs presented in Sec. 3 (i.e., fraction of each O species, Al coordination numbers, and Ca partial coordination numbers) to determine the state of rigidity of CAS glasses (i.e., flexible, isostatic, or stressed-rigid) as a function of temperature and composition by enumerating the number of radial BS and angular BB constraints per atom based on the coordination number of each atom, as described in the following. We first focus on the glassy state (i.e., low temperature). Table 3 summarizes the average number of BS and BB constraints created by each individual species in the glassy state. Note that, for simplicity, all the BS constraints are fully attributed to the cations (rather than being equally shared by cations and oxygen atoms). As expected, Si atoms systematically create 4 BS constraints with their 4 O neighbors, as well as 5 BB constraints (i.e., the minimum number of independent angles that need to be fixed to define the SiO_4 tetrahedron).[58] In contrast, Al atoms exhibit a varying coordination number (i.e., 4 or 5 herein), so that the number of BS constraints created by Al

atoms is given by their coordination number. Similar to Si atoms, 5 BB constraints are attributed to 4-fold Al atoms. However, we assume that 5-fold coordinated Al atoms do not create any BB constraints since they exhibit an unstable deformed octahedral angular environment.[53, 59–61] The enumeration of the topological constraints created by Ca atoms requires more attention considering the ionic nature of Ca–O bonds. First, since ionic Ca–O bonds are non-directional, Ca atoms do not exhibit any well-defined angular environments and, as such, do not create any BB constraints.[58] Second, since BO and TO atoms are already fully charge-compensated by their Si or Al neighbors, we assume that Ca atoms only create strong BS constraints with their surrounding FO and NBO neighbors. Finally, each BO atom creates 1 BB constraint (e.g., to maintain Si/Al–O–Si/Al angles fixed around their average values), while each TO atom creates 3 BB constraints to define its trigonal environment.[30] In contrast, FO and NBO atoms do not create any BB constraint due to the non-directional nature of ionic Ca–O bonds. Figure 5 illustrates the different atomic species that are present in CAS glasses, as well as their associated local environments. These inputs then serve to compute the number of BS and BB constraints for each glass composition.

Figure 6 presents the number of radial BS, angular BB, and total (BS+BB) number of constraints per atom (n_c) as a function of $[Al_2O_3]$ – [CaO] for the entire CAS domain. We first use the equations presented in Sec. 3 to determine the fraction of each type of O species as well as the coordination number of Al atoms (Eqs. 2-9). Based on these fractions, we then determine the partial coordination numbers of Ca atoms (Eqs. 10-to-12). Using all these topological inputs, we calculate the number of BS and BB constraints per atoms by following the information given in Tab. 3. The results obtained from our analytical topological model are compared with those obtained by MD simulations. We first note that the number of BS constraints per atom decreases upon increasing $[Al_2O_3]$ – [CaO], shows a minimum at $[Al_2O_3]$ = [CaO], and then subsequently increases [Fig. 6(a)]. The initial decrease in the number of BS constraints per atom primarily arises from the high number of BS constraints created by Ca atoms at low $[Al_2O_3]$ – [CaO], wherein most of the Ca atoms create 6 BS constraints with their surrounding NBO and FO atoms—thereby resulting in a glass that exhibits a large average coordination number. The average coordination number then decreases as Ca atoms get replaced by Al atoms. However, when $[Al_2O_3]$ > [CaO],

the increase in the fraction of 5-fold Al and TO atoms eventually results in an increase in the number of BS constraints per atom upon increasing $[Al_2O_3]$ – [CaO]. We then observe that the number BB constraints per atoms monotonically increases upon increasing $[Al_2O_3]$ – [CaO] [Fig. 6(b)]. This can be understood from the fact that atomic species which do not create any BB constraints (i.e., Ca, NBO, and FO) gradually disappear upon increasing $[Al_2O_3]$ – [CaO].

Altogether, we find that the total number of constraints per atom remains fairly constant (around n_c = 3) when $[Al_2O_3]$ < [CaO] and notably increases when $[Al_2O_3]$ > [CaO] [Fig. 6(c)]. This indicates that, at $[Al_2O_3]$ < [CaO], the decrease in the number of BS per atom is perfectly balanced by the increase in the number of BB per atom. This behavior agrees with previous findings obtained in densified silicate glasses, wherein the number of BB constraints was found to adapt to the number of BS constraints.[62] This behavior was attributed to a self-organization mechanism, wherein weaker angular constraints form or break in response to variations in the number of stronger radial constraints to ensure that the glass remains isostatic (n_c = 3).[63, 64]

Importantly, we find that our analytical topological model matches well with MD results. Note that, although the fractions of oxygen species [Fig. 3] and the Ca–O partial coordination numbers [Fig. 4] solely depend on $[Al_2O_3]$ – [CaO], the resulting number of constraints also depends on $[SiO_2]$ (which explains why the outcome of our model is represented as hatched areas in Fig. 6 rather than as a single line).

The resulting rigidity diagram for the CAS ternary system is shown in Fig. 7(a). We note that CAS glasses are found to be systematically rigid (i.e., isostatic or stressed-rigid, $n_c \geq 3$) irrespectively of composition. Notably, the ternary map of the number of constraints per atom closely mimics that of the Young's modulus of CAS glasses,[11] which supports the present constraint enumeration—since the Young's modulus has been shown to depend on the density of BS and BB constraints.[42] The increase in the rigidity of CAS glasses upon increasing $[Al_2O_3]$ – [CaO] also echoes the corresponding increase in glass transition temperature that is observed experimentally.[65, 66] Overall, our model offers an accurate description of the atomic structural rigidity for CAS glasses while remaining analytical.

2. Liquid state

Next, we discuss how temperature may affect the rigidity diagram of the CAS ternary system. To this end, we adopt temperature-dependent constraint theory, wherein each constraint can be intact (at low temperature, i.e., in the glassy state) or thermally-broken (at high temperature, i.e., in the liquid or supercooled liquid state) based on the competition between the constraints' free energy and available thermal energy.[67–69] Although that would be desirable, we are presently unable to accurately determine the onset temperature associated with each type of constraint in CAS glasses by means of MD simulations. More work is needed to establish a clear, robust criterion to discriminate intact from broken constraints. In the following, rather than relying on unproven guesses regarding the temperature at which constraints break, we simply discuss how the breaking of each type of constraint affects the rigidity diagram of the CAS ternary system, namely, the location of the flexible and stressed-rigid domains. These successive constraints enumerations simulate the effect of increasing temperature (i.e., which results in more and more constraints being broken).

In the following, we discuss the successive effects of the breaking of (a) O–Al–O BB constraints, (b) Ca–FO constraints, and (c) BO and TO BB constraints—wherein these constraints are tentatively ranked from the weakest to the strongest, that, these constraints are ranked in terms of the temperature at which they are expected to break. This ranking is based on the following observations. First, the angular BB constraints associated with 4-fold Al atoms have been suggested by many studies to be notably weaker than those associated with Si atoms.[27, 28, 70–73] This has been attributed to the fact that the nearby presence of a charge-compensating cation tends to destabilize the angular environment of 4-fold coordinated Al atoms.[28] Second, ionic Ca–FO constraints are expected to exhibit a low bond energy and, hence, to break at low temperature[68]. Finally, the BB constraints of BO and TO atoms (referred to as *γ* constraints) have been noted to break at low temperature.[68, 69] It is worth nothing that this ranking is only tentative, and more work is clearly needed to carefully determine the onset temperature at which each type of constraint breaks (and ranking thereof).

Figure 7 shows how the successive breaking of each type of constraint affects the rigidity diagram of the CAS ternary system. We first note that the breaking of the BB of the Al atoms

drastically affects the rigidity diagram and results in the appearance of a flexible domain ($n_c < 3$) in the SiO_2-poor and CaO-rich regions [Fig. 7(b)]. This suggests that CAS systems may exhibit a composition-driven rigidity transition (i.e., from flexible, $n_c < 3$, to stressed-rigid, $n_c > 3$) in this range of temperature. The subsequent breaking of the Ca–FO BS constraints plays, overall, a more minor effect, but drastically reduces the rigidity of CaO-rich compositions [Fig. 7(c)]. Finally, the breaking of the BO and TO BB constraints causes all the compositions to become flexible—at the notable exception of pure SiO_2, which becomes isostatic [Fig. 7(d)].

3. Correlations between network topology and glass/liquid properties

Interestingly, the ternary rigidity diagrams shown in Fig. 7 offer useful insights into the possible origin of the glass-forming ability of CAS systems. First, at the highest temperature considered herein [Fig. 7(d)], SiO_2 becomes perfectly isostatic ($n_c = 3$). This agrees with the excellent glass-forming ability of SiO_2.[19, 30] It should be noted that SiO_2 exhibits a high glass transition temperature, so that, unlike other silicate glasses, the topological origin of its glass-forming ability should indeed be assessed at high temperature (i.e., wherein the BB constraints of the BO atoms are thermally broken). The state of rigidity of the CAS ternary system at moderate temperature [Figs. 7(b) and 7(c)] also exhibits some correlations with glass-forming ability.[74, 75] First, CaO-rich systems are highly flexible ($n_c < 3$) and, hence—following Zachariasen's viewpoint[76]—do not have the ability to form an extended 3-dimensional rigid network to prevent crystallization. In contrast, Al_2O_3-rich glasses are highly stressed-rigid ($n_c > 3$). This may explain their low glass-forming ability, since the network does not exhibit enough structural flexibility to form a random (non-crystalline) network. The fact that SiO_2-rich calcium silicate glasses are stressed-rigid also echoes the fact that such glasses tend to phase-separate.[3, 74] It is also notable that the position of the isostatic boundary on the CaO–SiO_2 joint (around $(CaO)_{50}(SiO_2)_{50}$) corresponds to the compositional domain wherein calcium silicate glasses exhibit maximum glass-forming ability.[77] Altogether, these results suggest that it is the rigidity at finite temperature (i.e., in the supercooled liquid state) rather than at low temperature (i.e., in the glassy state) that governs the glass-forming ability of silicate glasses.

We further validate our model by exploring the existence of correlations between network topology and relevant glass/liquid experimental properties that have previously been suggested to be related to n_c. Here, we specially focus on experimental glass transition temperature, molar volume, and melt fragility data sourced from Bechgaard *et al.*[65] Molar volume are calculated using reported densities. Note that these data only cover a small portion of the CAS ternary—which prevents us from being fully conclusive.

Figure 8 shows the correlation between these properties and the number of constraints per atom n_c—wherein n_c is calculated by following the constraints enumeration assumptions used in Fig. 7b3 (i.e., wherein the BB of Al are considered broken). This choice is motivated from the fact that these properties are expected to be governed by the number of constraints per atom at moderate temperatures, that is, at temperatures slightly larger than T_g (in the supercooled liquid domain). Indeed, this is the range of temperatures that is relevant to describe the structure of the melt-forming glass during quenching, just before it freezes into a glass. This range of temperatures is expected (i) to govern the dynamical arrest that induces the glass transition (and, hence, that controls the value of T_g), (ii) to control the temperature-dependance of viscosity around T_g (as captured by the melt fragility index), and (iii) to describe the molar volume of the glass-forming melt as it freezes into a solid glass.

We first focus on the relationship between glass transition temperature (T_g) and number of constraints per atom n_c. Indeed, T_g has been suggested to be essentially a measure of the connectivity of the glass network.[78] As expected, we find T_g increases upon increases n_c [Fig. 8(a)], which echoes the fact that higher temperatures are needed to melt glasses that are more rigid (higher n_c)—since more topological constraints need to be thermally broken. Although we would need a more accurate knowledge of how the number of constraints depends on temperature to establish a quantitative relationship between T_g and atom n_c,[69, 79] we note that T_g exhibits a plateau in the flexible domain ($n_c < 3$). This kind of plateau has previously been observed in various oxide glasses and has been suggested to be associated to domains wherein the glass transition temperature becomes equal to the onset temperature of a specific constraint—that is, the temperature at which a given constraint thermally break.[67, 68, 79]

We then focus on the relationship between molar volume (V_m) and number of constraints per atom n_c. Indeed, it has previously been observed that ideally-connected isostatic glasses (especially chalcogenide glasses) exhibit an optimal space-filling tendency, which manifests itself as a minimum in molar volume.[80–86] Interestingly, we find that V_m exhibits a fair minimum around $n_c = 2.75$, which is close to the isostatic threshold [Fig. 8(b)]. This suggests that the optimal space-filling tendency of isostatic glasses might a be generic feature of the glassy state.

Last, we check the relationship between the melt fragility index (m) and number of constraints per atom n_c. This is motivated from the fact that several chalcogenide and oxide glasses have been noted to exhibit a minimum in melt fragility around their isostatic threshold.[82–87] Although the lack of available experimental data prevents us from being fully conclusive, we do observe a strong correlation between m and n_c—wherein flexible glasses ($n_c < 3$) exhibit larger fragility values than their isostatic counterparts [Fig. 8(c)]. Additional measurements in the stressed-rigid domains ($n_c > 3$) would be needed to test the existence of a minimum of fragility in this system.

5. Conclusion

This work establishes a sound model describing the network topology of CAS glasses as a function of their compositions. It is important to note that, although this model is informed and validated by MD simulations, it remains fully analytical and, hence, can bypass MD simulations to offer predictions of the topology of a given CAS glass based on the sole knowledge of its composition. Indeed, this model provides a direct access to the state of rigidity (flexible, isostatic, or stressed-rigid) of CAS glasses as a function of composition and temperature regime (which dictates if a certain constraint species is thermally active or not). The obtained temperature-dependent ternary rigidity diagrams reveal the existence of correlations between network topology and glass-forming ability—wherein highly underconstrained (flexible) and highly overconstrained (stressed-rigid) systems exhibit low glass-forming ability, while, in turn, optimally-constrained glasses (isostatic) feature maximum glass-forming ability. Importantly, this study suggests that glass-forming ability is encoded in the network topology of the liquid state rather than that of the glassy state.

It should be noted that, in general, a meaningful modeling exercise should attempt to describe a complex reality in the simplest fashion. Simplicity is especially important in the case of the topological design of glasses, since analytical models make it possible to offer direct predictions of the compositional dependence of glass properties. In turn, analytical models are differentiable and, hence, can be used for gradient-informed optimization approaches or to analytically predict which composition will maximize a given property. In that regard, although our model indeed relies on a certain number of assumptions, it eventually offers an excellent description of the number of bond-stretching and bond-bending constraints as a function of composition. As such, we believe that our model achieves a good balance between accuracy and simplicity, and, hence, can be used as a guide to identifying promising glass compositions.

Note that the modeling approach presented herein is based on generic physical/chemical behaviors (e.g., based on charge-balance, etc.). As such, we anticipate that our modeling approach could be used to analytically predict and extrapolate the topology of other families of silicate glasses, without the need for systematic MD simulations.

Acknowledgments

This work was supported by the National Science Foundation (under Grants No. 1762292, 1826420, 1826050, 1928538, and 1944510) and the Federal Highway Administration (Grant #: 693JJ31950021).

References

1. Ellison A, Cornejo IA. Glass Substrates for Liquid Crystal Displays. *International Journal of Applied Glass Science*. 2010;1(1):87–103. https://doi.org/10.1111/j.2041-1294.2010.00009.x
2. Taylor HFW. Cement Chemistry. Thomas Telford; 1997
3. Huang C, Behrman EC. Structure and properties of calcium aluminosilicate glasses. *Journal of Non-Crystalline Solids*. 1991;128(3):310–321. https://doi.org/10.1016/0022-3093(91)90468-L

4. Cormier L, Neuville DR, Calas G. Structure and properties of low-silica calcium aluminosilicate glasses. *Journal of Non-Crystalline Solids*. 2000;274(1):110–114. https://doi.org/10.1016/S0022-3093(00)00209-X
5. Neuville DR, Cormier L, Massiot D. Al coordination and speciation in calcium aluminosilicate glasses: Effects of composition determined by 27Al MQ-MAS NMR and Raman spectroscopy. *Chemical Geology*. 2006;229(1):173–185. https://doi.org/10.1016/j.chemgeo.2006.01.019
6. Hennet L, Drewitt JWE, Neuville DR, *et al.* Neutron diffraction of calcium aluminosilicate glasses and melts. *Journal of Non-Crystalline Solids*. 2016;451:89–93. https://doi.org/10.1016/j.jnoncrysol.2016.05.018
7. Ganster P, Benoit M, Kob W, Delaye J-M. Structural properties of a calcium aluminosilicate glass from molecular-dynamics simulations: A finite size effects study. *J Chem Phys*. 2004;120(21):10172–10181. https://doi.org/10.1063/1.1724815
8. Bouhadja M, Jakse N, Pasturel A. Structural and dynamic properties of calcium aluminosilicate melts: a molecular dynamics study. *J Chem Phys*. 2013;138(22):224510. https://doi.org/10.1063/1.4809523
9. Dai X, He J, Bai J, *et al.* Ash Fusion Properties from Molecular Dynamics Simulation: Role of the Ratio of Silicon and Aluminum. *Energy Fuels*. 2016;30(3):2407–2413. https://doi.org/10.1021/acs.energyfuels.5b02586
10. Jabraoui H, Badawi M, Lebègue S, Vaills Y. Elastic and structural properties of low silica calcium aluminosilicate glasses from molecular dynamics simulations. *Journal of Non-Crystalline Solids*. 2018;499:142–152. https://doi.org/10.1016/j.jnoncrysol.2018.07.004
11. Yang K, Xu X, Yang B, *et al.* Predicting the Young's Modulus of Silicate Glasses using High-Throughput Molecular Dynamics Simulations and Machine Learning. *Scientific Reports*. 2019;9(1):8739. https://doi.org/10.1038/s41598-019-45344-3
12. Ravinder R, Sridhara KH, Bishnoi S, *et al.* Deep learning aided rational design of oxide glasses. *Mater Horiz*. 2020;7(7):1819–1827. https://doi.org/10.1039/D0MH00162G
13. Hu Y-J, Zhao G, Zhang M, *et al.* Predicting densities and elastic moduli of SiO_2-based glasses by machine learning. *npj Computational Materials*. 2020;6(25):1–13. https://doi.org/10.1038/s41524-020-0291-z

14. Varshneya AK, Mauro JC. Fundamentals of Inorganic Glasses. Elsevier; 2019 https://doi.org/10.1016/C2017-0-04281-7
15. Zanotto ED, Coutinho FAB. How many non-crystalline solids can be made from all the elements of the periodic table? *Journal of Non-Crystalline Solids*. 2004;347(1):285–288. https://doi.org/10.1016/j.jnoncrysol.2004.07.081
16. Liu H, Du T, Krishnan NMA, Li H, Bauchy M. Topological optimization of cementitious binders: Advances and challenges. *Cement and Concrete Composites*. 2019;101:5–14. https://doi.org/10.1016/j.cemconcomp.2018.08.002
17. Mauro JC. Decoding the glass genome. *Current Opinion in Solid State and Materials Science*. 2018;22(2):58–64. https://doi.org/10.1016/j.cossms.2017.09.001
18. Mauro JC, Tandia A, Vargheese KD, Mauro YZ, Smedskjaer MM. Accelerating the Design of Functional Glasses through Modeling. *Chem Mater*. 2016;28(12):4267–4277. https://doi.org/10.1021/acs.chemmater.6b01054
19. Phillips JC. Topology of covalent non-crystalline solids I: Short-range order in chalcogenide alloys. *Journal of Non-Crystalline Solids*. 1979;34(2):153–181. https://doi.org/10.1016/0022-3093(79)90033-4
20. Thorpe MF. Continuous deformations in random networks. *Journal of Non-Crystalline Solids*. 1983;57(3):355–370. https://doi.org/10.1016/0022-3093(83)90424-6
21. Phillips JC. Topology of covalent non-crystalline solids II: Medium-range order in chalcogenide alloys and A-Si(Ge). *Journal of Non-Crystalline Solids*. 1981;43(1):37–77. https://doi.org/10.1016/0022-3093(81)90172-1
22. Bauchy M. Deciphering the atomic genome of glasses by topological constraint theory and molecular dynamics: A review. *Computational Materials Science*. 2019;159:95–102. https://doi.org/10.1016/j.commatsci.2018.12.004
23. Mauro JC, Ellison AJ, Allan DC, Smedskjaer MM. Topological Model for the Viscosity of Multicomponent Glass-Forming Liquids. *International Journal of Applied Glass Science*. 2013;4(4):408–413. https://doi.org/10.1111/ijag.12009

24. Smedskjaer MM, Mauro JC, Youngman RE, Hogue CL, Potuzak M, Yue Y. Topological Principles of Borosilicate Glass Chemistry. *J Phys Chem B*. 2011;115(44):12930–12946. https://doi.org/10.1021/jp208796b
25. Smedskjaer MM. Topological Model for Boroaluminosilicate Glass Hardness. *Front Mater*. 2014;1:23. https://doi.org/10.3389/fmats.2014.00023
26. Bauchy M, Wang B, Wang M, *et al.* Fracture toughness anomalies: Viewpoint of topological constraint theory. *Acta Materialia*. 2016;121:234–239. https://doi.org/10.1016/j.actamat.2016.09.004
27. Pignatelli I, Kumar A, Bauchy M, Sant G. Topological Control on Silicates' Dissolution Kinetics. *Langmuir*. 2016;32(18):4434–4439. https://doi.org/10.1021/acs.langmuir.6b00359
28. Liu H, Zhang T, Anoop Krishnan NM, *et al.* Predicting the dissolution kinetics of silicate glasses by topology-informed machine learning. *npj Materials Degradation*. 2019;3:32. https://doi.org/10.1038/s41529-019-0094-1
29. Mauro JC. Topological constraint theory of glass. *American Ceramic Society Bulletin*. 2011;90(4):31.
30. Bauchy M. Topological Constraint Theory and Rigidity of Glasses. *arXiv:200504603 [cond-mat]*. 2019. https://doi.org/10.1201/9780367333003
31. Le Losq C, Neuville DR, Florian P, Henderson GS, Massiot D. The role of Al3+ on rheology and structural changes in sodium silicate and aluminosilicate glasses and melts. *Geochimica et Cosmochimica Acta*. 2014;126:495–517. https://doi.org/10.1016/j.gca.2013.11.010
32. McMillan PF, Kirkpatrick RJ. Al coordination in magnesium aluminosilicate glasses. *American Mineralogist*. 1992;77(7–8):898–900.
33. Stebbins JF, Kroeker S, Keun Lee S, Kiczenski TJ. Quantification of five- and six-coordinated aluminum ions in aluminosilicate and fluoride-containing glasses by high-field, high-resolution 27Al NMR. *Journal of Non-Crystalline Solids*. 2000;275(1):1–6. https://doi.org/10.1016/S0022-3093(00)00270-2
34. Bauchy M. Structural, vibrational, and elastic properties of a calcium aluminosilicate glass from molecular dynamics simulations: The role of the potential. *The Journal of Chemical Physics*. 2014;141(2):024507. https://doi.org/10.1063/1.4886421

35. Nesbitt HW, Bancroft GM, Henderson GS, *et al.* Bridging, non-bridging and free (O2–) oxygen in Na2O-SiO2 glasses: An X-ray Photoelectron Spectroscopic (XPS) and Nuclear Magnetic Resonance (NMR) study. *Journal of Non-Crystalline Solids*. 2011;357(1):170–180. https://doi.org/10.1016/j.jnoncrysol.2010.09.031
36. Nesbitt HW, Bancroft GM, Henderson GS, Sawyer R, Secco RA. Direct and indirect evidence for free oxygen (O2−) in MO-silicate glasses and melts (M = Mg, Ca, Pb). *American Mineralogist*. 2015;100(11–12):2566–2578. https://doi.org/10.2138/am-2015-5336
37. Cormier L, Ghaleb D, Neuville DR, Delaye J-M, Calas G. Chemical dependence of network topology of calcium aluminosilicate glasses: a computer simulation study. *Journal of Non-Crystalline Solids*. 2003;332(1):255–270. https://doi.org/10.1016/j.jnoncrysol.2003.09.012
38. Schoenholz SS, Cubuk ED. JAX, M.D.: End-to-End Differentiable, Hardware Accelerated, Molecular Dynamics in Pure Python. *arXiv:191204232 [cond-mat, physics:physics, stat]*. 2019.
39. Plimpton S. Fast Parallel Algorithms for Short-Range Molecular Dynamics. *Journal of Computational Physics*. 1995;117(1):1–19. https://doi.org/10.1006/jcph.1995.1039
40. Yu Y, Wang B, Lee YJ, Bauchy M. Fracture Toughness of Silicate Glasses: Insights from Molecular Dynamics Simulations. *MRS Online Proceedings Library Archive*. 2015;1757. https://doi.org/10.1557/opl.2015.50
41. Wang B, Yu Y, Lee YJ, Bauchy M. Intrinsic Nano-Ductility of Glasses: The Critical Role of Composition. *Front Mater*. 2015;2:11. https://doi.org/10.3389/fmats.2015.00011
42. Yang K, Yang B, Xu X, Hoover C, Smedskjaer MM, Bauchy M. Prediction of the Young's modulus of silicate glasses by topological constraint theory. *Journal of Non-Crystalline Solids*. 2019;514:15–19. https://doi.org/10.1016/j.jnoncrysol.2019.03.033
43. Fennell CJ, Gezelter JD. Is the Ewald summation still necessary? Pairwise alternatives to the accepted standard for long-range electrostatics. *The Journal of Chemical Physics*. 2006;124(23):234104. https://doi.org/10.1063/1.2206581
44. Li X, Song W, Yang K, *et al.* Cooling rate effects in sodium silicate glasses: Bridging the gap between molecular dynamics simulations and experiments. *The Journal of Chemical Physics*. 2017;147(7):074501. https://doi.org/10.1063/1.4998611

45. Martínez L, Andrade R, Birgin EG, Martínez JM. PACKMOL: a package for building initial configurations for molecular dynamics simulations. *J Comput Chem*. 2009;30(13):2157–2164. https://doi.org/10.1002/jcc.21224
46. Le Losq C, Cicconi MR, Greaves GN, Neuville DR. Silicate Glasses. In: Musgraves JD, Hu J, Calvez L, eds. *Springer Handbook of Glass*. Cham: Springer International Publishing; 2019:441–503. https://doi.org/10.1007/978-3-319-93728-1_13
47. Day DE, Rindone GE. Properties of Soda Aluminosilicate Glasses: Coordination of Aluminum Ions. *Journal of the American Ceramic Society*. 1962;45(12):579–581. https://doi.org/10.1111/j.1151-2916.1962.tb11063.x
48. Taylor TD, Rindone GE. Properties of Soda Aluminosilicate Glasses: V, Low-Temperature Viscosities. *Journal of the American Ceramic Society*. 1970;53(12):692–695. https://doi.org/10.1111/j.1151-2916.1970.tb12044.x
49. McKeown DA, Galeener FL, Brown GE. Raman studies of Al coordination in silica-rich sodium aluminosilicate glasses and some related minerals. *Journal of Non-Crystalline Solids*. 1984;68(2):361–378. https://doi.org/10.1016/0022-3093(84)90017-6
50. Riebling EF. Structure of Sodium Aluminosilicate Melts Containing at Least 50 mole % SiO2 at 1500°C. *J Chem Phys*. 1966;44(8):2857–2865. https://doi.org/10.1063/1.1727145
51. Stukowski A. Visualization and analysis of atomistic simulation data with OVITO–the Open Visualization Tool. *Modelling Simul Mater Sci Eng*. 2010;18:015012. https://doi.org/10.1088/0965-0393/18/1/015012
52. Wayne Nesbitt H, Henderson GS, Michael Bancroft G, Sawyer R, Secco RA. Bridging oxygen speciation and free oxygen (O2−) in K-silicate glasses: Implications for spectroscopic studies and glass structure. *Chemical Geology*. 2017;461:13–22. https://doi.org/10.1016/j.chemgeo.2016.11.026
53. Xiang Y, Du J, Smedskjaer MM, Mauro JC. Structure and properties of sodium aluminosilicate glasses from molecular dynamics simulations. *J Chem Phys*. 2013;139(4):044507. https://doi.org/10.1063/1.4816378

54. Iuga D, Morais C, Gan Z, Neuville DR, Cormier L, Massiot D. NMR Heteronuclear Correlation between Quadrupolar Nuclei in Solids. *J Am Chem Soc*. 2005;127(33):11540–11541. https://doi.org/10.1021/ja052452n
55. Takahashi S, Neuville DR, Takebe H. Thermal properties, density and structure of percalcic and peraluminus CaO–Al2O3–SiO2 glasses. *Journal of Non-Crystalline Solids*. 2015;411:5–12. https://doi.org/10.1016/j.jnoncrysol.2014.12.019
56. Toplis MJ, Dingwell DB, Lenci T. Peraluminous viscosity maxima in Na2O Al2O3 SiO2 liquids: The role of triclusters in tectosilicate melts. *Geochimica et Cosmochimica Acta*. 1997;61(13):2605–2612. https://doi.org/10.1016/S0016-7037(97)00126-9
57. Eckersley MC, Gaskell PH, Barnes AC, Chieux P. Structural ordering in a calcium silicate glass. *Nature*. 1988;335(6190):525–527. https://doi.org/10.1038/335525a0
58. Bauchy M, Abdolhosseini Qomi MJ, Bichara C, Ulm F-J, Pellenq RJ-M. Nanoscale Structure of Cement: Viewpoint of Rigidity Theory. *J Phys Chem C*. 2014;118(23):12485–12493. https://doi.org/10.1021/jp502550z
59. Stebbins JF, Wu J, Thompson LM. Interactions between network cation coordination and non-bridging oxygen abundance in oxide glasses and melts: Insights from NMR spectroscopy. *Chemical Geology*. 2013;346:34–46. https://doi.org/10.1016/j.chemgeo.2012.09.021
60. Burnham CW, Buerger MJ. Refinement of the crystal structure of andalusite. *Zeitschrift für Kristallographie - Crystalline Materials*. 1961;115(3–4):269–290. https://doi.org/10.1524/zkri.1961.115.3-4.269
61. Lucovsky G. Transition from thermally grown gate dielectrics to deposited gate dielectrics for advanced silicon devices: A classification scheme based on bond ionicity. *Journal of Vacuum Science & Technology A*. 2001;19(4):1553–1561. https://doi.org/10.1116/1.1379317
62. Bauchy M, Micoulaut M. Densified network glasses and liquids with thermodynamically reversible and structurally adaptive behaviour. *Nature Communications*. 2015;6(1):6398. https://doi.org/10.1038/ncomms7398
63. Bauchy M, Micoulaut M. Transport Anomalies and Adaptative Pressure-Dependent Topological Constraints in Tetrahedral Liquids: Evidence for a Reversibility Window

Analogue. *Phys Rev Lett*. 2013;110(9):095501. https://doi.org/10.1103/PhysRevLett.110.095501

64. Bauchy M, Qomi MJA, Bichara C, Ulm F-J, Pellenq RJ-M. Rigidity Transition in Materials: Hardness is Driven by Weak Atomic Constraints. *Phys Rev Lett*. 2015;114(12):125502. https://doi.org/10.1103/PhysRevLett.114.125502
65. Bechgaard TK, Mauro JC, Bauchy M, *et al.* Fragility and configurational heat capacity of calcium aluminosilicate glass-forming liquids. *Journal of Non-Crystalline Solids*. 2017;461:24–34. https://doi.org/10.1016/j.jnoncrysol.2017.01.033
66. Cormier L, Neuville DR, Calas G. Relationship Between Structure and Glass Transition Temperature in Low-silica Calcium Aluminosilicate Glasses: the Origin of the Anomaly at Low Silica Content. *Journal of the American Ceramic Society*. 2005;88(8):2292–2299. https://doi.org/10.1111/j.1551-2916.2005.00428.x
67. Gupta PK, Mauro JC. Composition dependence of glass transition temperature and fragility. I. A topological model incorporating temperature-dependent constraints. *J Chem Phys*. 2009;130(9):094503. https://doi.org/10.1063/1.3077168
68. Mauro JC, Gupta PK, Loucks RJ. Composition dependence of glass transition temperature and fragility. II. A topological model of alkali borate liquids. *J Chem Phys*. 2009;130(23):234503. https://doi.org/10.1063/1.3152432
69. Bauchy M, Micoulaut M. Atomic scale foundation of temperature-dependent bonding constraints in network glasses and liquids. *Journal of Non-Crystalline Solids*. 2011;357(14):2530–2537. https://doi.org/10.1016/j.jnoncrysol.2011.03.017
70. Oey T, Hsiao Y-H, Callagon E, *et al.* Rate controls on silicate dissolution in cementitious environments. *RILEM Technical Letters*. 2017;2:67–73. https://doi.org/10.21809/rilemtechlett.2017.35
71. Oey T, Kumar A, Pignatelli I, *et al.* Topological controls on the dissolution kinetics of glassy aluminosilicates. *Journal of the American Ceramic Society*. 2017;100(12):5521–5527. https://doi.org/10.1111/jace.15122

72. Oey T, Callagon E, Falzone G, *et al.* Topological controls on aluminosilicate glass dissolution: Complexities induced in hyperalkaline aqueous environments. *J AM CERAM SOC*. 2020;103(11):6198–6207.
73. Gin S, Wang M, Bisbrouck N, *et al.* Can a simple topological-constraints-based model predict the initial dissolution rate of borosilicate and aluminosilicate glasses? *npj Materials Degradation*. 2020;4:6. https://doi.org/10.1038/s41529-020-0111-4
74. Martel L, Allix M, Millot F, *et al.* Controlling the Size of Nanodomains in Calcium Aluminosilicate Glasses. *J Phys Chem C*. 2011;115(39):18935–18945. https://doi.org/10.1021/jp200824m
75. Shelby JE. Formation and Properties of Calcium Aluminosilicate Glasses. *Journal of the American Ceramic Society*. 1985;68(3):155–158. https://doi.org/10.1111/j.1151-2916.1985.tb09656.x
76. Zachariasen WH. The Atomic Arrangement in Glass. *J Am Chem Soc*. 1932;54(10):3841–3851. https://doi.org/10.1021/ja01349a006
77. Saravanapavan P, Hench LL. Mesoporous calcium silicate glasses. I. Synthesis. *Journal of Non-Crystalline Solids*. 2003;318(1):1–13. https://doi.org/10.1016/S0022-3093(02)01864-1
78. Micoulaut M. Glass Transition Temperature Variation as a Probe for Network Connectivity. In: Thorpe MF, Phillips JC, eds. *Phase Transitions and Self-Organization in Electronic and Molecular Networks*. Boston, MA: Springer US; 2001:143–160. https://doi.org/10.1007/0-306-47113-2_10
79. Hu Y, Liu Z, Yang K, *et al.* Rigidity theory of glass: Determining the onset temperature of topological constraints by molecular dynamics. *Journal of Non-Crystalline Solids*. 2021;554:120614. https://doi.org/10.1016/j.jnoncrysol.2020.120614
80. Rompicharla K, Novita DI, Chen P, Boolchand P, Micoulaut M, Huff W. Abrupt boundaries of intermediate phases and space filling in oxide glasses. *J Phys: Condens Matter*. 2008;20(20):202101. https://doi.org/10.1088/0953-8984/20/20/202101
81. Zhou Q, Wang M, Guo L, Boolchand P, Bauchy M. Intermediate Phase in Calcium–Silicate–Hydrates: Mechanical, Structural, Rigidity, and Stress Signatures. *Front Mater*. 2019;6. https://doi.org/10.3389/fmats.2019.00157

82. Chbeir R, Bauchy M, Micoulaut M, Boolchand P. Evidence for a Correlation of Melt Fragility Index With Topological Phases of Multicomponent Glasses. *Front Mater*. 2019;6. https://doi.org/10.3389/fmats.2019.00173
83. Welton A, Chbeir R, McDonald M, *et al.* Unusual Role of P–P Bonds on Melt Dynamics and Topological Phases of the Equimolar GexPxSe100–2x Glass System. *J Phys Chem C*. 2020;124(45):25087–25106. https://doi.org/10.1021/acs.jpcc.0c07491
84. Chakravarty S, Almutairi BS, Chbeir R, *et al.* Progress, Challenges, and Rewards in Probing Melt Dynamics, Configurational Entropy Change, and Topological Phases of Group V- and Group IV-Based Multicomponent Sulfide Glasses. *physica status solidi (b)*. 2020;257(11):2000116. https://doi.org/10.1002/pssb.202000116
85. Mohanty C, Mandal A, Gogi VK, *et al.* Linking Melt Dynamics With Topological Phases and Molecular Structure of Sodium Phosphate Glasses From Calorimetry, Raman Scattering, and Infrared Reflectance. *Front Mater*. 2019;6. https://doi.org/10.3389/fmats.2019.00069
86. Chakravarty S, Chbeir R, Chen P, Micoulaut M, Boolchand P. Correlating Melt Dynamics and Configurational Entropy Change With Topological Phases of AsxS100–x Glasses and the Crucial Role of Melt/Glass Homogenization. *Front Mater*. 2019;6. https://doi.org/10.3389/fmats.2019.00166
87. Boolchand P, Bauchy M, Micoulaut M, Yildirim C. Topological Phases of Chalcogenide Glasses Encoded in the Melt Dynamics. *physica status solidi (b)*. 2018;255(6):1800027. https://doi.org/10.1002/pssb.201800027

List of Figure Captions

Figure 1. Atomic snapshots of (a) $(CaO)_{25}(SiO_2)_{75}$, (b) $(CaO)_{50}(SiO_2)_{50}$, and (c) $(CaO)_{25}(Al_2O_3)_{25}(SiO_2)_{50}$ glasses obtained from molecular dynamics simulations. O, Si, Al, and Ca atoms are colored in red, yellow, gray, and purple, respectively. Bond cutoffs are 2.000 and 2.345 Å for Si–O and Al–O pairs, respectively. All snapshots are 5 Å thick slices obtained using OVITO.[51]

Figure 2. Predicted (from the analytical model) and computed (from molecular dynamics simulations) numbers of 5-fold Al atoms per formula unit of glasses as a function of composition. Results are plotted as a function of the difference between the molar fractions of the Al_2O_3 and CaO oxides in the glass ("$[Al_2O_3]$ – [CaO]"). The right-side positive domain (i.e., $[Al_2O_3]$ – [CaO] > 0) corresponds to Al-rich compositions, while the left-side negative domain ($[Al_2O_3]$ – [CaO] < 0) corresponds to Ca-rich compositions. Note that several CAS glass compositions are associated with the same $[Al_2O_3]$ – [CaO] value.

Figure 3. Predicted (from the analytical model) and computed (from molecular dynamics simulations) fractions of each type of oxygen species as a function of composition: (a) free oxygen (FO), (b) non-bridging oxygen (NBO), (c) bridging oxygen (BO), and (d) "tricluster" oxygen (TO). Results are plotted as a function of the difference between the molar fractions of the Al_2O_3 and CaO oxides in the glass ("$[Al_2O_3]$ – [CaO]"). The right-side positive domain (i.e., $[Al_2O_3]$ – [CaO] > 0) corresponds to Al-rich compositions, while the left-side negative domain ($[Al_2O_3]$ – [CaO] < 0) corresponds to Ca-rich compositions.

Figure 4. Predicted (from analytical model) and computed (from molecular dynamics simulations) values of the (a) Ca–FO, (b) Ca–NBO, (c) Ca–BO, and (d) Ca–TO partial coordination numbers of Ca atoms as a function of composition. Results are plotted as a function of the difference between the molar fractions of the Al_2O_3 and CaO oxides in the glass ("$[Al_2O_3]$ – [CaO]"). The right-side positive domain (i.e., $[Al_2O_3]$ – [CaO] > 0) corresponds to Al-rich compositions, while the left-side negative domain ($[Al_2O_3]$ – [CaO] < 0) corresponds to Ca-rich compositions.

Figure 5. Illustrations of the number of bond-stretching (BS) and bond-bending (BB) constraints created by (a) 4-fold Si, (b) 4-fold Al, (c) 5-fold Al, (d) Ca, (e) free oxygen (FO), (f) non-bridging oxygen (NBO), (g) bridging oxygen (BO), and (h) tri-cluster oxygen (TO) atoms. O, Si, Al, and Ca atoms are colored in red, yellow, gray, and purple, respectively. All snapshots are obtained by OVITO.[51]

Figure 6. Predicted (from analytical model) and computed (from molecular dynamics simulations) (a) number of bond-stretching (BS), (b) number of bond-bending (BB), and (c) total number of constraints per atom (n_c) as a function of composition. Results are plotted as a function of the difference between the molar fractions of the Al_2O_3 and CaO oxides in the glass ("$[Al_2O_3]$ – [CaO]"). The right-side positive domain (i.e., $[Al_2O_3]$ – [CaO] > 0) corresponds to Al-rich compositions, while the left-side negative domain ($[Al_2O_3]$ – [CaO] < 0) corresponds to Ca-rich compositions. The red area indicates the number of constraints in the glasses associated with a fixed value of $[Al_2O_3]$ – [CaO], since several glasses with different compositions (and, hence, different number of constraints) can be associated with the same $[Al_2O_3]$ – [CaO] value.

Figure 7. Ternary plots presenting the number of (1) radial bond-stretching (BS), (2) angular bond-bending (BB), and (3) total number of constraints (n_c) per atom predicted by our analytical topological model. The constraints enumeration is conducted at (a) room temperature (glassy state), (b) the temperature at which O–Al–O BB constraints break, (c) the temperature at which Ca–FO BS constraints break, and (d) the temperature at which BO and TO BB constraints break. The solid black line in the n_c ternary maps (b3 and c3) indicates the location of the flexible-to-rigid transition (i.e., at $n_c = 3$).

Figure 8. Experimental values of (a) glass transition temperature T_g, (b) molar volume V_m, and (c) melt fragility index m as a function of the number of constraints per atom n_c (calculated for the range of

temperature considered in Fig. 7(b3). Experimental data are sourced from Bechgaard *et al*.[65] Note that these data points only cover a small portion of the $CaO–Al_2O_3–SiO_2$ (CAS) ternary system.

Table 1 Coefficients of the Jakse potential.[8] The superscripts indicate the partial charge of each element.

Pair	A_{ij} (kcal/mol)	σ_{ij} (Å)	ρ_{ij} (Å)	C_{ij} (kcal/mol Å^6)
$O^{-1.2}–O^{-1.2}$	0.276344	3.6430	0.2630	1959.372
$O^{-1.2}–Si^{2.4}$	0.16120	2.5419	0.1560	1066.0667
$O^{-1.2}–Al^{1.8}$	0.172715	2.6067	0.1640	796.2097
$O^{-1.2}–Ca^{1.2}$	0.17732	2.9935	0.1780	793.0907
$Si^{2.4}–Si^{2.4}$	0.0276344	1.4408	0.0460	580.030
$Si^{2.4}–Al^{1.8}$	0.0575717	1.5056	0.0570	433.2063
$Si^{2.4}–Ca^{1.2}$	0.062177	1.8924	0.0630	529.445489
$Al^{1.8}–Al^{1.8}$	0.066783	1.5704	0.0680	323.548
$Al^{1.8}–Ca^{1.2}$	0.073691778	1.9572	0.0740	395.425476
$Ca^{1.2}–Ca^{1.2}$	0.080600	2.3440	0.0800	483.27068

Table 2 Summary of the predicted fractions of oxygen species in $(CaO)_x(Al_2O_3)_y(SiO_2)_{1-x-y}$ glasses, where x and y represent the mole percent of [CaO] and [Al_2O_3], respectively. f_{FO}, f_{NBO}, f_{BO}, and f_{TO} are the fractions of free oxygen (FO), non-bridging oxygen (NBO), bridging oxygen (BO), and tricluster oxygen (TO) atoms, respectively. Equations are separated into three distinct compositional regimes as discussed in the text.

	Fully-depolymerized regime	Partially-depolymerized regime	Fully-polymerized regime
Regime condition:	$(y - x) \leq -\frac{2}{3}$	$-\frac{2}{3} \leq (y - x) \leq 0$	$0 \leq (y - x)$

f_{FO}	$\frac{-2-3(y-x)}{2+(y-x)}$	0	0
f_{NBO}	$\frac{4+4(y-x)}{2+(y-x)}$	$\frac{-2(y-x)}{2+(y-x)}$	0
f_{BO}	0	$\frac{2+3(y-x)}{2+(y-x)}$	$\frac{4-3(y-x)}{4+2(y-x)}$
f_{TO}	0	0	$\frac{5(y-x)}{4+2(y-x)}$

Table 3 Summary of the number of radial bond-stretching (BS) and angular bond-bending (BB) constraints created by each atomic species in calcium aluminosilicate glasses (at low temperature). For Al and O atoms, the BS and BB constraints are distinguished in terms of their coordination numbers. Note that the constraints created by Ca atoms depend on the type of O atoms they are connected to.

	Glassy state	
Species	BS	BB
Si atoms	4	5
Al atoms		
4-fold Al	4	5
5-fold Al	5	0
Ca–O bonds		
Ca–FO	1	/
Ca–NBO	1	/
Ca–BO	0	/
Ca–TO	0	/
O atoms		
FO	/	0
NBO	/	0
BO	/	1
TO	/	3

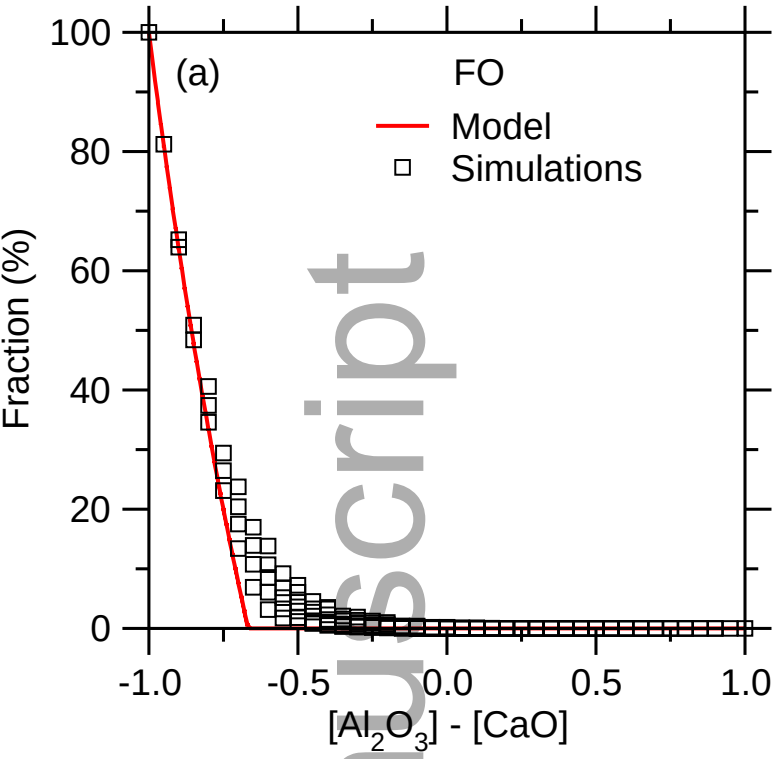

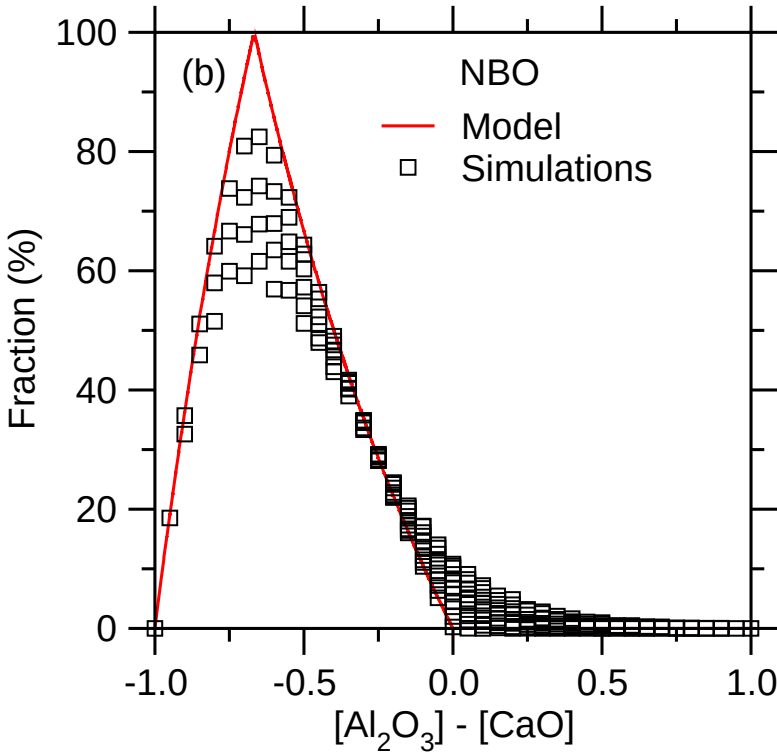

jace_17781_f3ab.eps

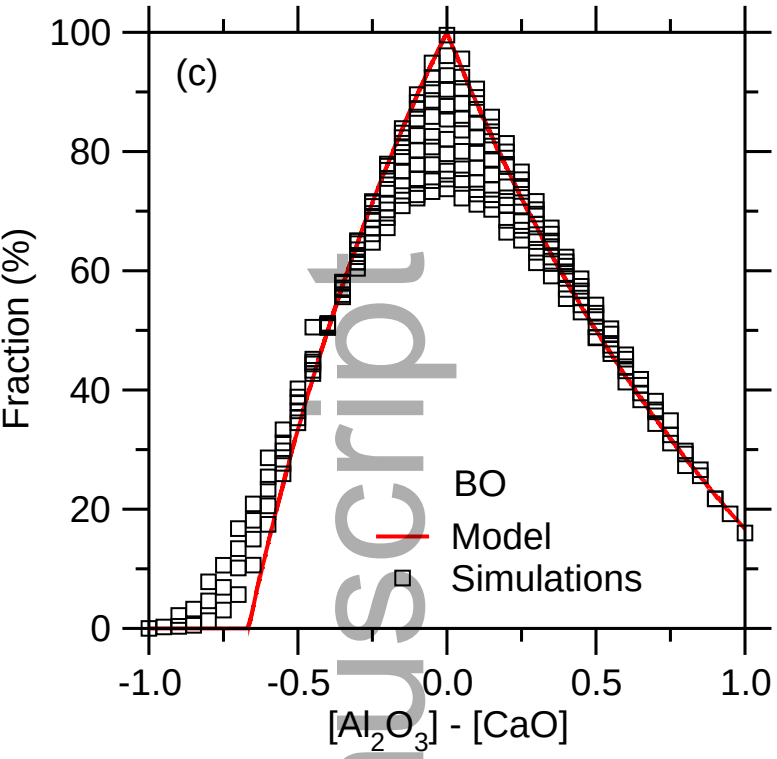

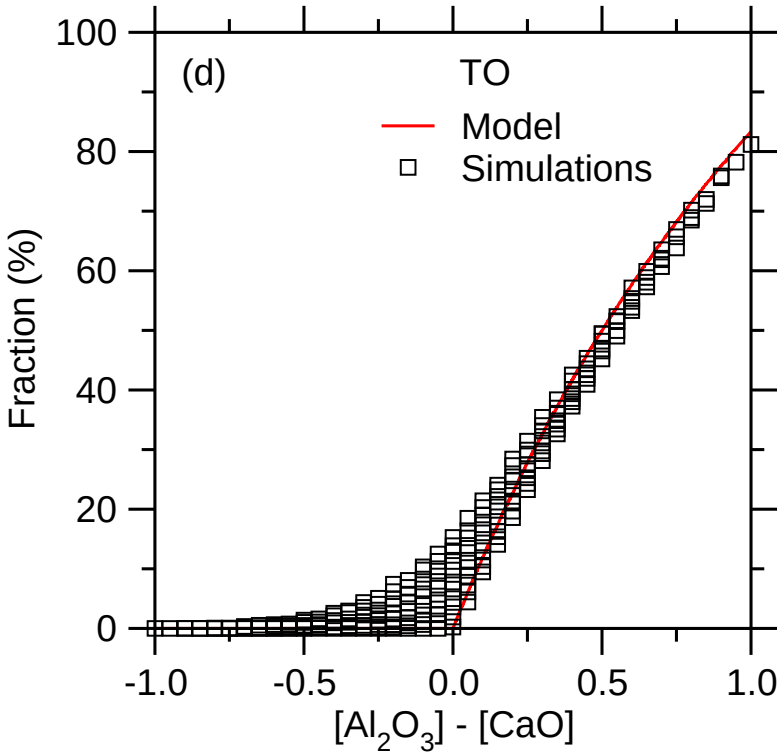

jace_17781_f3cd.eps

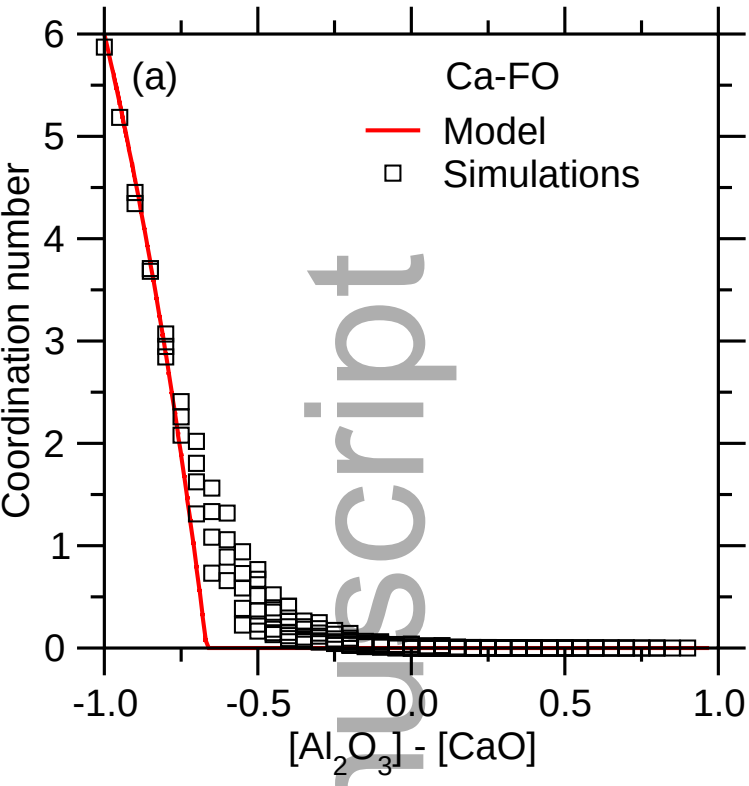

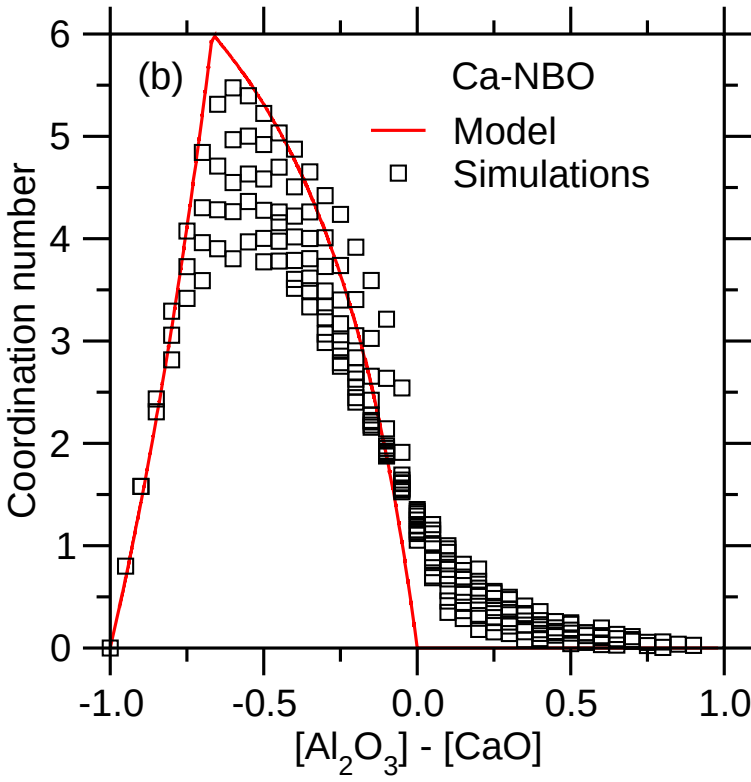

jace_17781_f4ab.eps

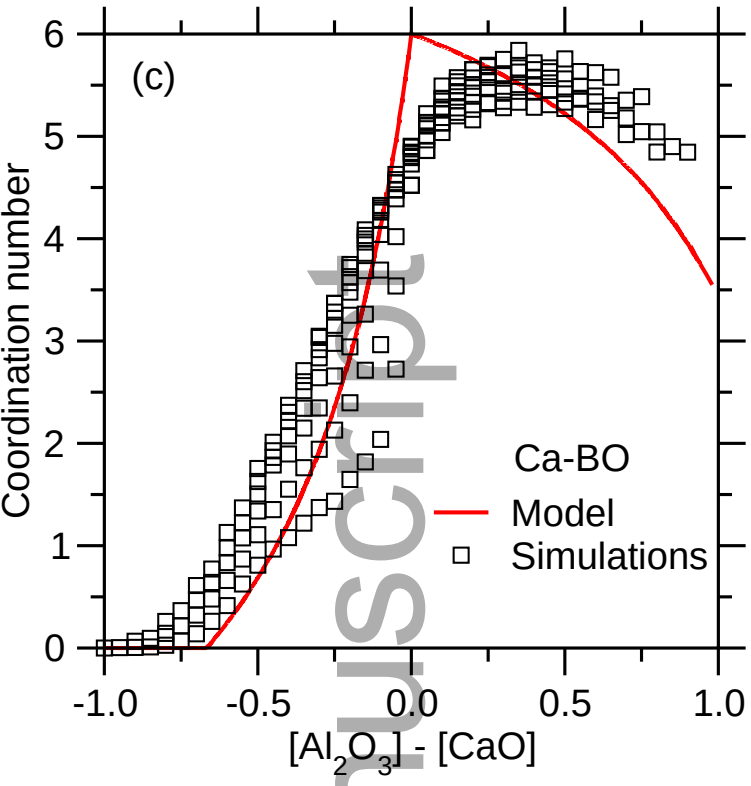

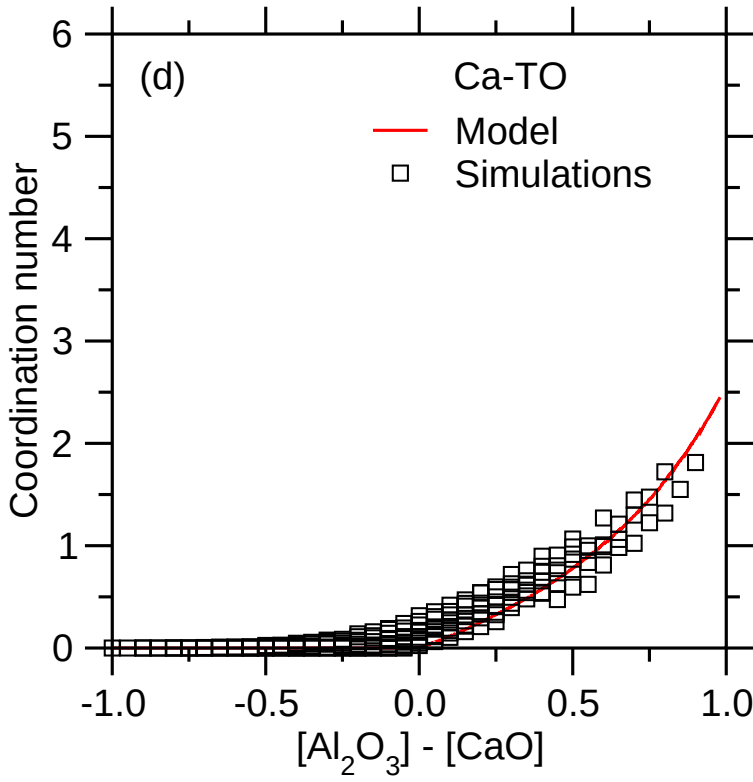

jace_17781_f4cd.eps

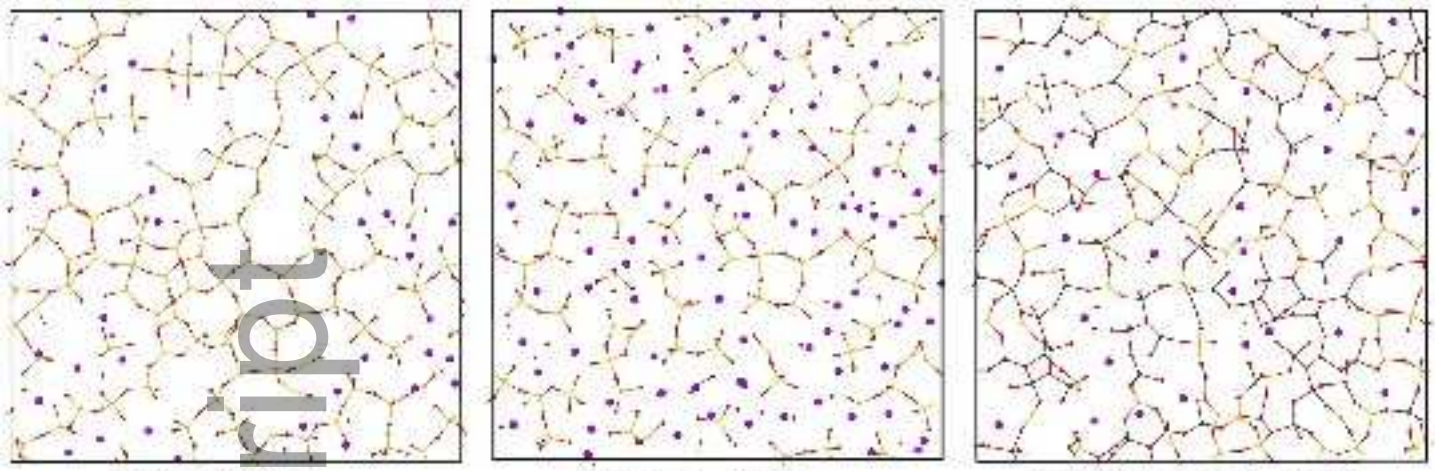

(a) $(CaO)_{25}(SiO_2)_{75}$ (b) $(CaO)_{50}(SiO_2)_{50}$ (c) $(CaO)_{25}(Al_2O_3)_{25}(SiO_2)_{50}$

jace_17781_f1.jpg

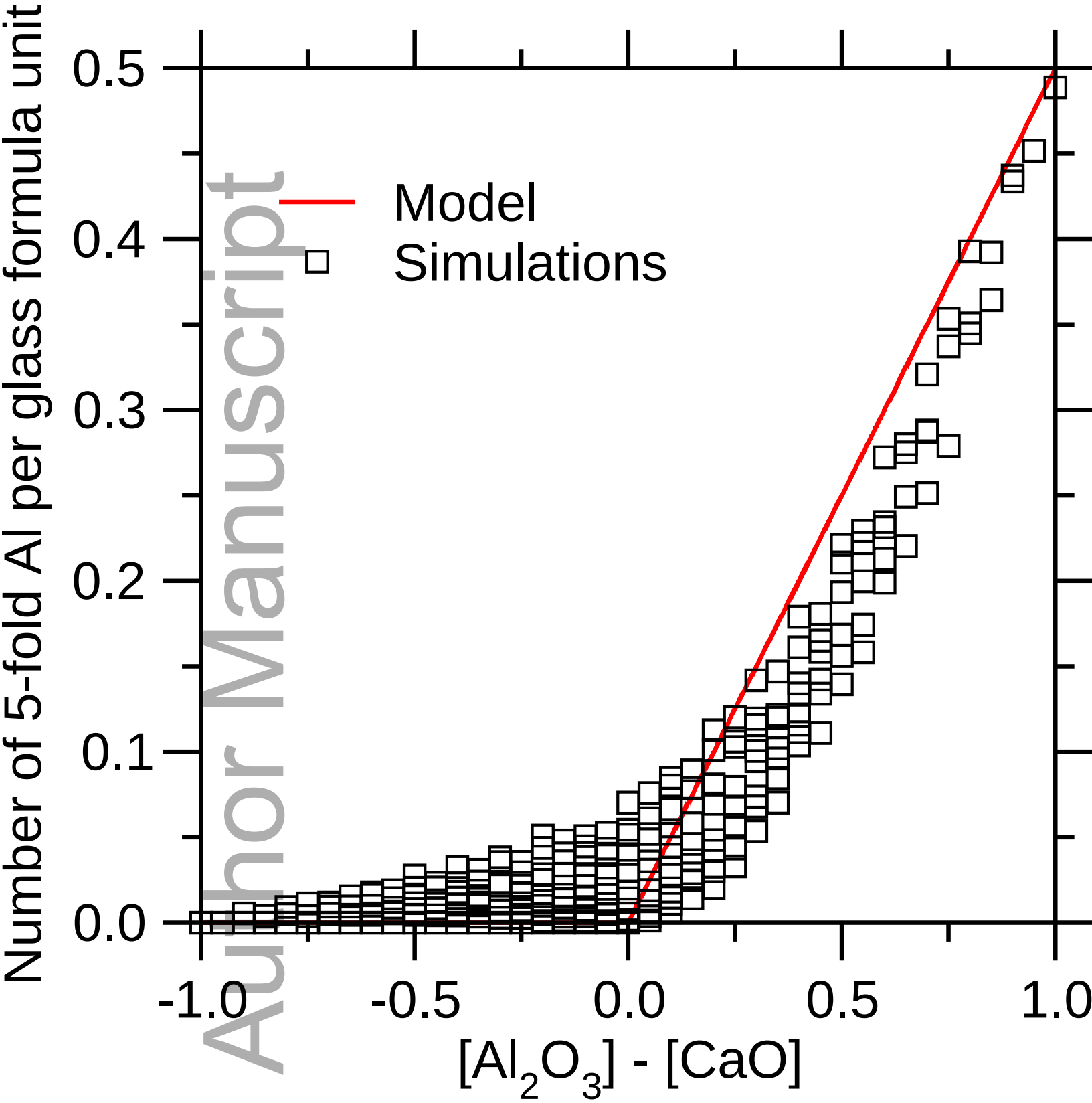

jace_17781_f2.eps

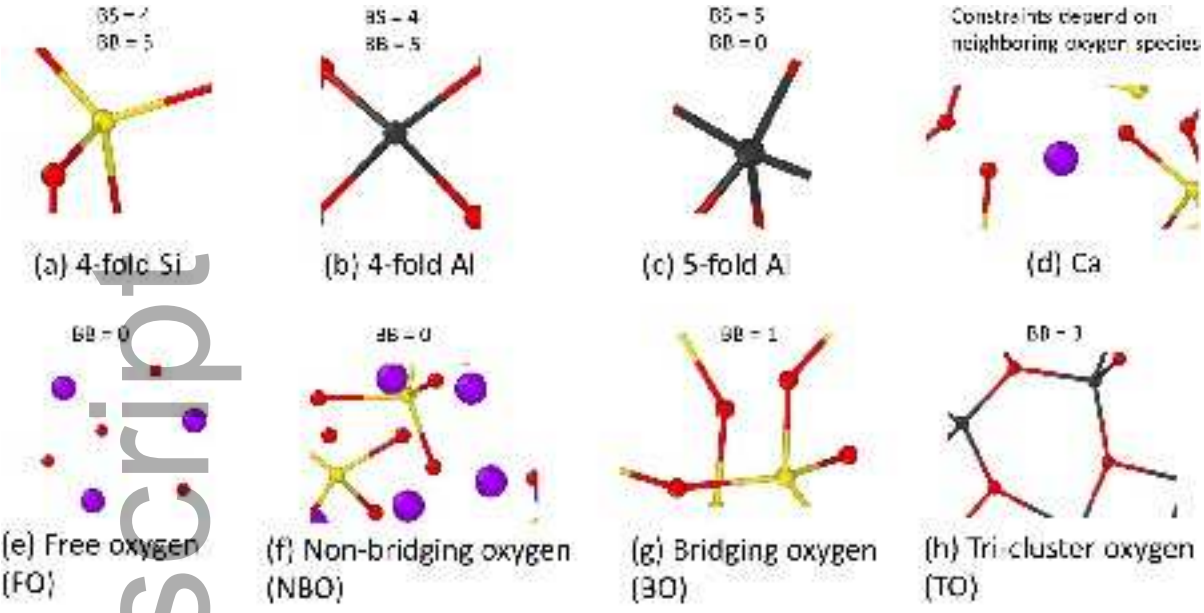

jace_17781_f5.jpg

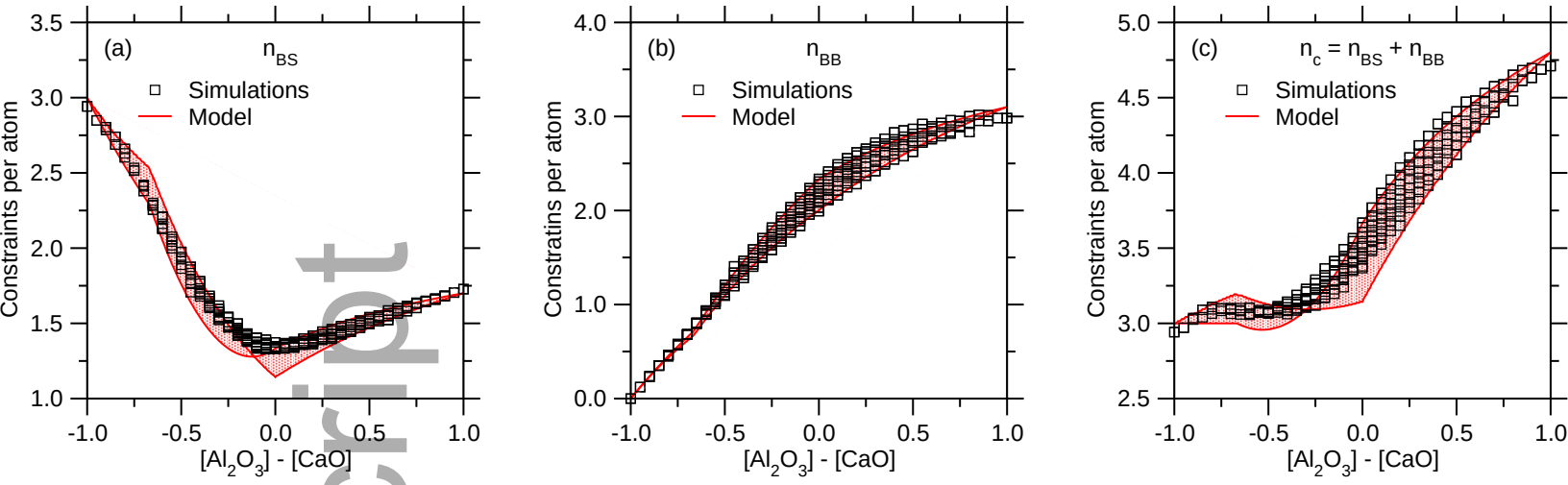

jace_17781_f6.eps

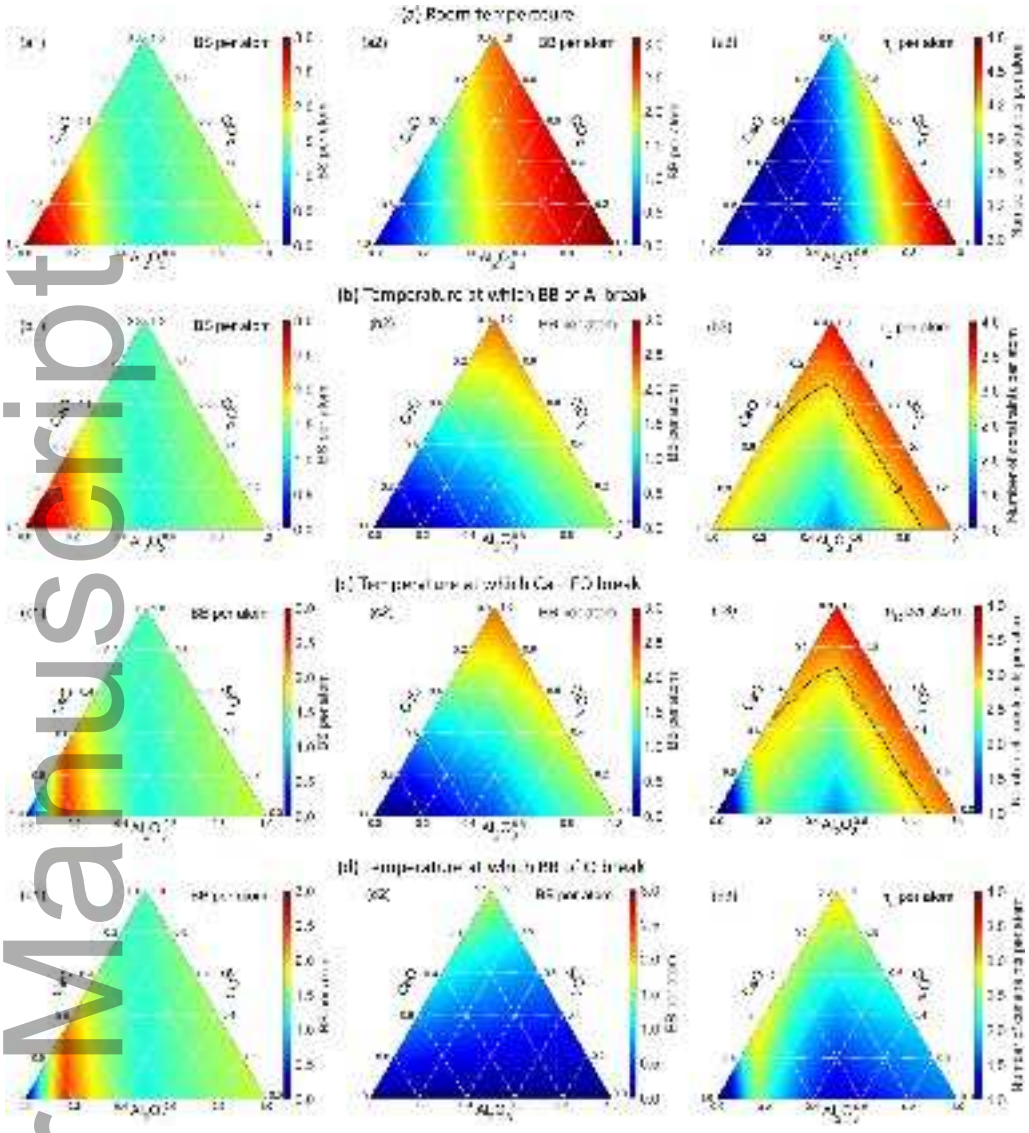

jace_17781_f7.jpg

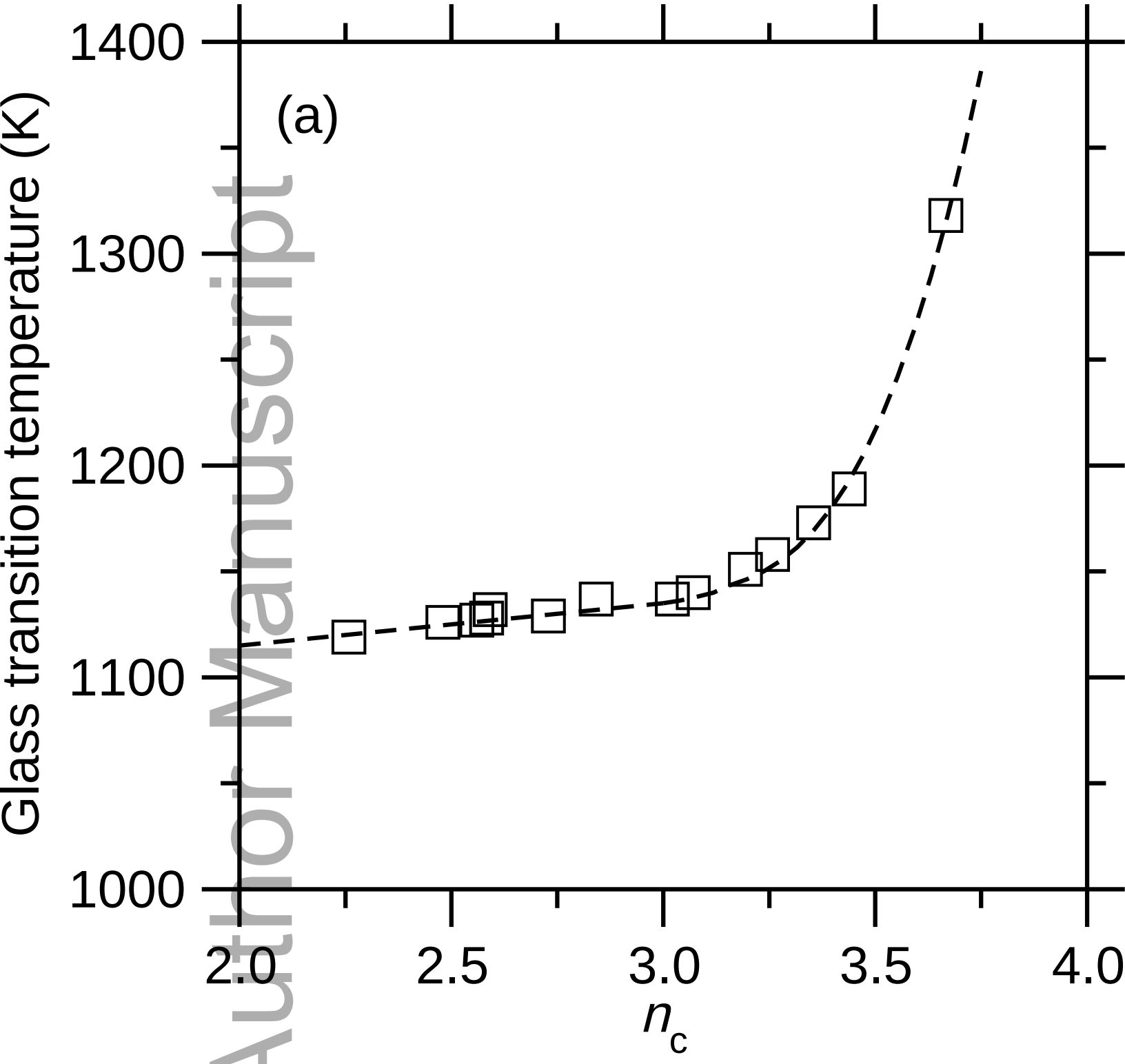

jace_17781_f8a.eps

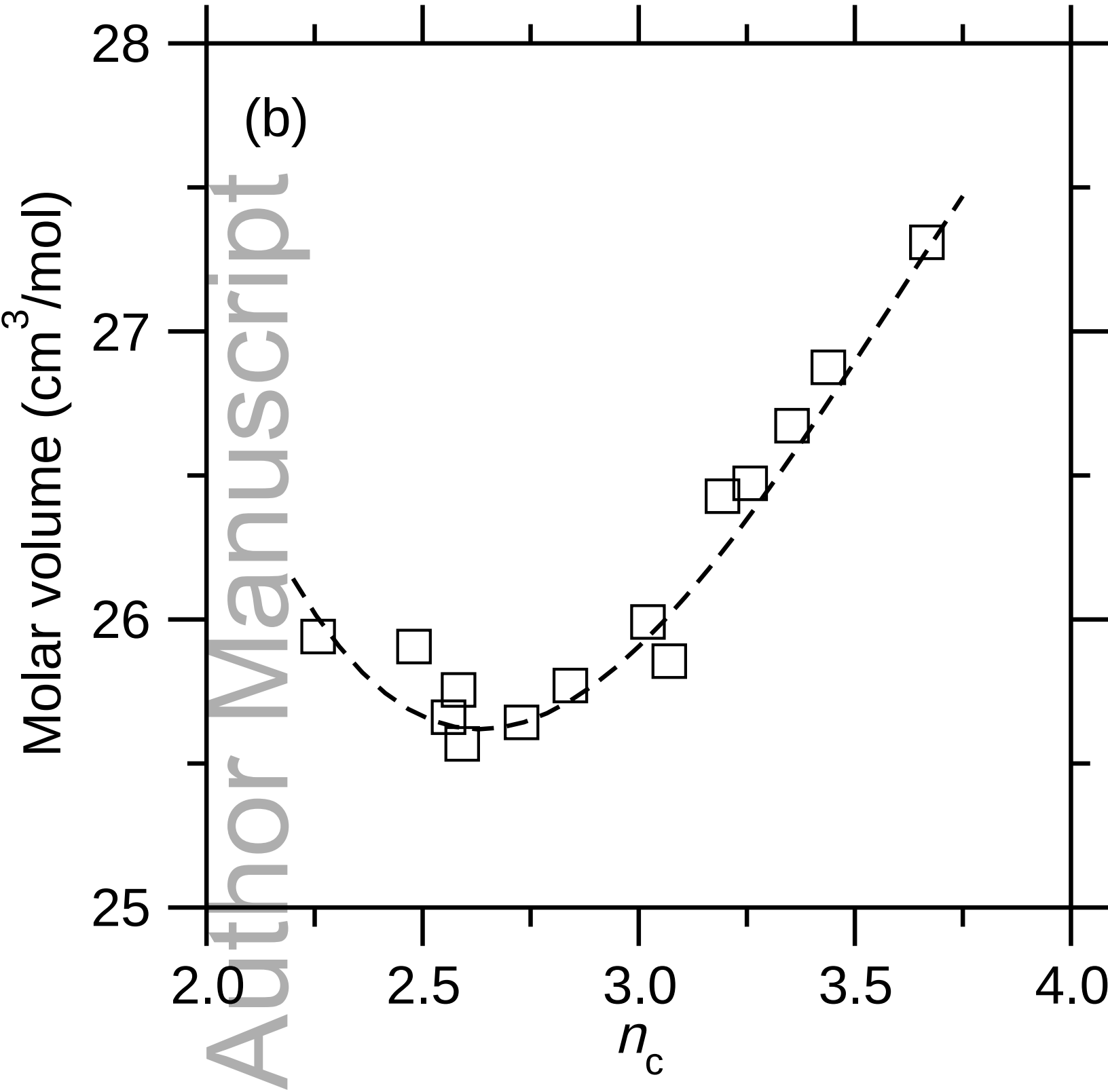

jace_17781_f8b.eps

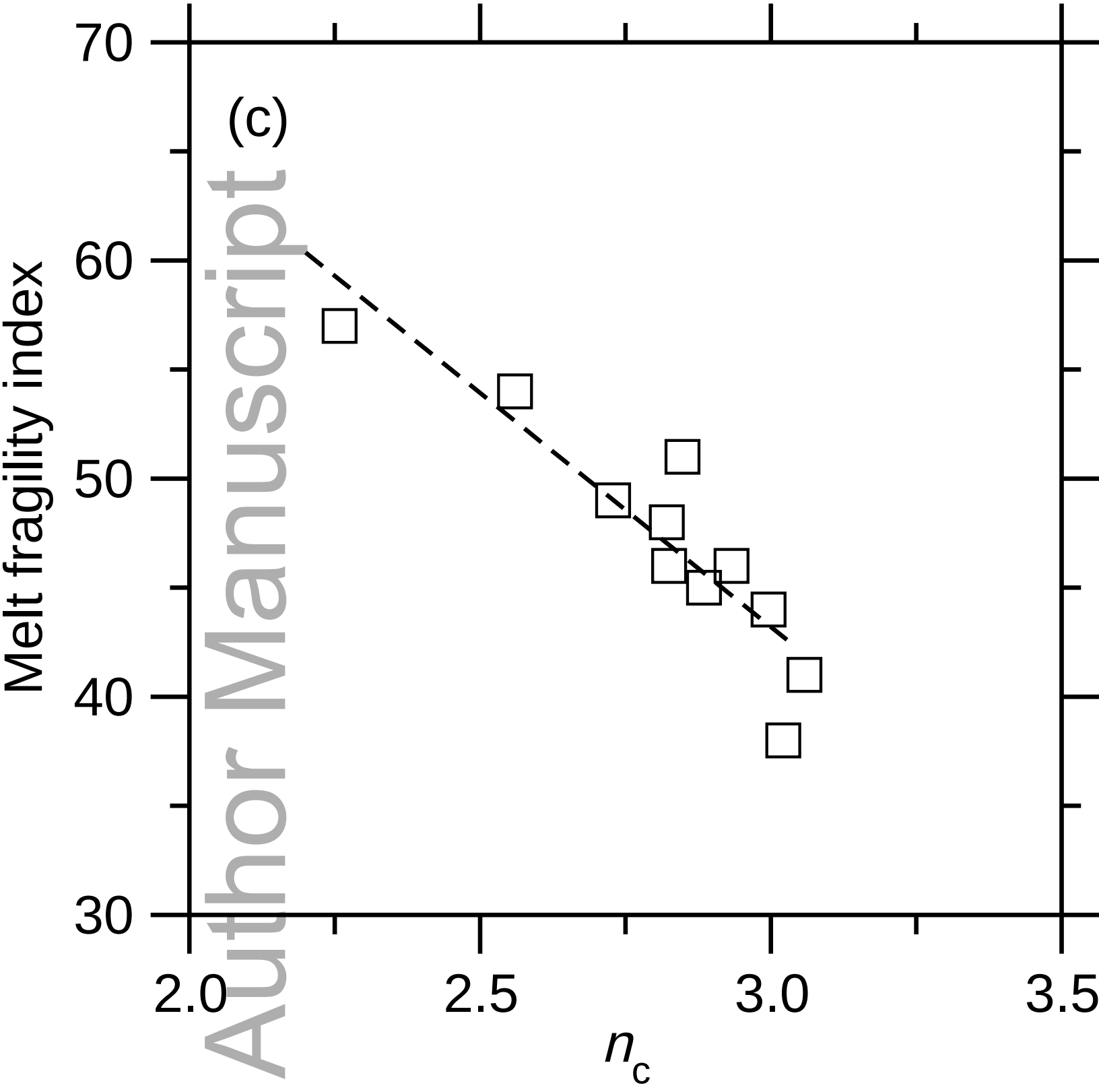

jace_17781_f8c.eps